Journal of Magnetism and Magnetic Materials 622 (2025) 172954

Contents lists available at ScienceDirect

Journal of Magnetism and Magnetic Materials

journal homepage: www.elsevier.com/locate/jmmm

Research article

Remanent magnetic response of hard magnetorheological elastomer foams: Fabrication, microstructure characterization and modeling

Zehui Lin, Zahra Hooshmand-Ahoor, Kostas Danas *, Laurence Bodelot *

Laboratoire de Mécanique des Solides (LMS), CNRS, Ecole Polytechnique, Institut Polytechnique de Paris, Route de Saclay, 91128, Palaiseau Cedex, France

ARTICLE INFO

Keywords:
Magnetorheological elastomer (MRE)
Silicone foams
Hard magnetic particles
Ellipsoidal pores
Magnetization
Remanent magnetic field

ABSTRACT

This work deals with the experimental, numerical and theoretical study of the purely magnetic response of hard magnetorheological elastomer (*h*-MRE) foams of variable particle and porosity content. First, the fabrication and experimental measurement of the remanent magnetic flux of the *h*-MRE foams are presented. We find that at lower particle content, the foam comprises closed-cell porosity, with the voids having a variable size and ellipsoidal shape. As the particle content in the matrix increases, the voids become smaller in size and more spherical in shape, while the porosity decreases. We show experimentally that the remanent magnetic flux is entirely independent of the shape and orientation of the voids. Image-based morphological analysis of the *h*-MRE foam microstructure subsequently allows to reconstruct numerically unit-cells that share the same statistics as those of the experimental foams. These unit-cells are used to construct an explicit theoretical model with magnetic dissipation. We show that the remanent magnetization is a linear function of the overall particle volume fraction in the foam. The model is further used to scale up the analysis and solve the experimental boundary value problem of a permanently magnetized *h*-MRE cube, and the numerical estimates show excellent agreement with the experiments. Finally, the numerical model is shown to match available analytical solutions for the remanent magnetic flux of parallelepiped magnets.

1. Introduction

Magnetorheological elastomers (MREs) are smart composite materials comprising magnetic micron-sized particles embedded in polymer matrices. They have attracted widespread attention because of their capability to deform substantially under small to medium applied magnetic fields [1–11], but also because they can take complex shapes allowing for functionality by design [12,13]. Currently, MREs may be further divided in two main families: magnetically soft (*s*-MRE) or hard (*h*-MRE) depending on the magnetic properties of the filler particles. Specifically, *s*-MREs contain particles that do not retain magnetization upon removal of the magnetic field (e.g., carbonyl iron powder (CIP)), while *h*-MREs contain particles that exhibit remanent magnetization upon field removal (e.g., NdFeB) [14–18]. Applications of such smart materials range from vibration absorbers [19–21], isolators [22,23], cell migration control [24] to soft robots [16,25–27] among others.

From a different perspective, MRE foams [28] have gained increased interest too. Indeed, they are lightweight [29,30], have increased magnetostriction performance [31], show larger magnetorheological (MR) effect than pure MREs [32], and their fabrication under magnetic field can be leveraged to impart anisotropic mechanical properties to the material [33]. MRE foams reported in the literature can be produced in two distinct ways [34]. The so-called "ex-situ" method consists in filling the pores of an existing foam with an MRE (or a magnetorheological fluid) blend [35,36]. However, most studies are dedicated to "in-situ" foams, which are generally obtained by dispersing the particles in the constituent material and adding a foaming (or blowing) agent to create pores during the polymerization process [31,34].

Furthermore, research on in-situ MRE foams has nearly exclusively focused on polyurethane foams filled with CIP. These *s*-MRE foams exhibit a rather high modulus (a few hundred kPa [29]) as well as a regular pore structure with pore sizes below a few hundred microns [37], which makes them appropriate for applications in the tunable absorption of shocks [38] and sound [39]. Works on these foams have extensively addressed their morphological [40,41], rheological [42], magnetic [43] and magneto-mechanical [37,44] properties.

In contrast, very few works have considered softer elastomer foam matrices [28,45,46] and, to the best of the authors' knowledge, *h*-MRE foams have not been investigated yet. *h*-MRE foam would exhibit a remanent magnetic field owing to the fact that hard magnetic particles retain magnetization, which soft magnetic particles do not. Hence, exploiting concurrently the lightweight property of the foam and the

* Corresponding authors.
E-mail addresses: konstantinos.danas@polytechnique.edu (K. Danas), laurence.bodelot@polytechnique.edu (L. Bodelot).

https://doi.org/10.1016/j.jmmm.2025.172954
Received 3 December 2024; Received in revised form 14 February 2025; Accepted 10 March 2025
Available online 18 March 2025

Table 1
Elemental composition of the magnetic particles.

Element	Boron (B)	Iron (Fe)	Cerium (Ce)	Praseodymium (Pr)	Neodymium (Nd)
wt%	1	75.1	6.4	0.3	17.2

remanent magnetic field could be of great interest in designing ultra-light soft sensors, soft actuators or programmable soft robots [27,47]. Thus, this study proposes to investigate the fabrication process of *h*-MRE soft foams, its influence on the foam morphology and pore distribution, as well as the influence of the magnetization amplitude on the purely magnetic remanent behavior of the obtained foams. Further insight is built by confronting experimental results to numerical simulations. While the present study only focuses on the purely magnetic response, it constitutes a first necessary step fabrication-wise but also modeling-wise for the understanding of the more complete coupled magneto-mechanical response of these materials. The later is underway and is left for the future.

2. Fabrication of *h*-MRE soft foams

2.1. Raw materials and fabrication process

The material used in this study is Soma Foama 25 (Smooth-On, USA), a soft two-component flexible platinum silicone foam. When the two components (Part A and Part B) are combined, the mixture generates bubbles, leading to a 2–3 times increase of the original volume.

The hard magnetic particles are in a form of powder (MQFP-12-5-20092-089, Neo Magnequench, China), whose composition is indicated in Table 1. In particular, the manufacturer reports isotropic particles, with sizes in the range 1.38–26.16 μm, a mean volume diameter (MV) of 5.28 μm. Most of the magnetic properties of the particles are taken from previous studies [17,48] whereas their magnetization saturation is calibrated by use of one experimental data point in this study, as discussed in detail in Section 5.3.

For the fabrication, we first disperse the particles in Part B (which is the most viscous component) along with Silicon Thinner fluid (Smooth-On, USA) to lower the overall viscosity and promote a homogeneous dispersion of the particles. The compound is thoroughly hand-mixed for 15 s. Then, we add Part A, and mix again for 15 s before pouring the mixture in a mold previously sprayed with a release agent (Ease Release 200, Smooth-On, USA) in order to facilitate the removal of the sample after curing. Curing takes place at room temperature for 1 h.

The relative quantity of particles in the polymer blend is expressed in parts per hundred rubber (phr) defined as

$$phr = 100\,\frac{M_p}{M_A + M_B} \qquad \text{or} \qquad M_p = \frac{phr}{100}\,(M_A + M_B). \tag{1}$$

In this relation, M_p (in g) corresponds to the mass of particles and $M_A + M_B$ (with $M_A = M_B$ in the present work) is the two-component silicon mass in liquid form. Note that in all cases, the silicon thinner has mass 5 wt% of $M_A + M_B$.

2.2. Influence of the mold shape on the foam morphology

Next, we 3D print two molds with Verowhite material (Stratasys, USA): the first mold has a constant cross-section of 10 mm × 10 mm and a total height of 15 mm, while the second mold has a 10 mm × 10 mm cross-section along a 15 mm height followed by a 15 mm × 15 mm cross-section along another 15 mm height. Since constrained foaming has been observed to reduce MR foam porosity [49], we carry out all tests allowing for free foaming, i.e, by leaving the top of the molds open. *h*-MRE foam mixtures of 70, 140 and 210 phr are poured in each mold up to 15 mm. The entirety of the obtained samples are cut vertically in the middle to observe their cross-section with a VH-Z20R microscope (Keyence, Japan) under 30x magnification. In the micrographs reported in Fig. A.13, the contour of the mold is indicated in red, and the considered zone of interest, a 10 mm × 10 mm square (to later yield a cubic sample) is delineated in blue.

In all cases, though much less markedly for the 210 phr samples, the pores are of ellipsoidal shape and mostly elongated in the upward direction of foaming. With the first mold, the ellipsoidal pores located at the top of the mold tend to tilt towards the center as the foam freely exits the mold and creates an enlarged dome at the top. With the second mold, where the expansion of the foam is laterally constrained by the 15 mm × 15 mm cross-section chimney of 15 mm height at the exit of the 10 mm × 10 mm cross-section, the tilt of the pores towards the center is much less marked. As a result, since the pore shapes appear more uniform in the zone of interest, all samples are subsequently fabricated using the second mold.

Then, we fabricate two series of samples each with 70, 140 and 210 phr and we make either a vertical or horizontal mid cut using a razor blade to obtain cross-sections for pore characterization, as discussed in detail in Section 3. Next, we fabricate and characterize magnetically (see Section 4) 10 additional samples with 70, 140 and 210 phr, which are cut in cubes of volume $V_f = 10 \times 10 \times 10$ mm^3 and mass M_f (denoted here for later use).

3. Morphological characterization of *h*-MRE foams

3.1. Porosity and particle volume fraction estimates

During the fabrication process, the masses of the raw components (particles and uncured silicone) and phr serve as the control parameters. Nevertheless, the main parameter affecting the final magnetic response is the total volume fraction of particles in the *h*-MRE foam. For this reason, we proceed here with an approximate estimation of the relevant volume fractions of the components making up the foam, i.e., the volume fraction of the voids, c_v, the pure silicon matrix, c_s, the particles in the *h*-MRE matrix (comprising the particles and the silicon but not the voids), c_{pm}, and the particles in the entire foam, c_p.

Following the concomitant curing and formation of voids, volume fractions of the particles and voids in the *h*-MRE are estimated by *assuming* that the silicon matrix mass and volume in liquid and cured form are conserved.[1] Considering next the addition of 5 wt% silicon thinner in the entire mixture and Eq. $(1)_2$, one may approximate the mass of the *cured* silicon M_s and thus that of the particles M_p by

$$M_s \simeq 1.05\,(M_A + M_B), \qquad M_p = \frac{phr}{105}\,M_s. \tag{2}$$

Using these last relations together with the standard identities

$$V_f = V_v + V_p + V_s, \quad M_f = M_p + M_s,\ M_v = 0, \quad \rho_{(f,s,p)} = \frac{M_{(f,s,p)}}{V_{(f,s,p)}} \tag{3}$$

we get after some straightforward algebra (using $M_f = (phr/105+1)M_s$ that the volume fraction of voids c_v in the foam sample is given by

$$c_v = \frac{V_v}{V_f} = 1 - \frac{V_p + V_s}{V_f} = 1 - \frac{\rho_f\,(phr\,\rho_s + 105\,\rho_p)}{\rho_s\,\rho_p(105 + phr)}. \tag{4}$$

Here, $\rho_f = M_f/V_f$, ρ_s and ρ_p denote the densities of the *h*-MRE foam, the silicon matrix phase and the particles, respectively. In particular,

[1] This assumption is extremely difficult to verify in the present case, where the foaming process starts immediately after mixing parts A and B. Even so, we use this usual approximation which allows us to describe eventually the magnetic response of the *h*-MRE foam as a function of the particle volume fraction which theoretically is the most relevant quantity.

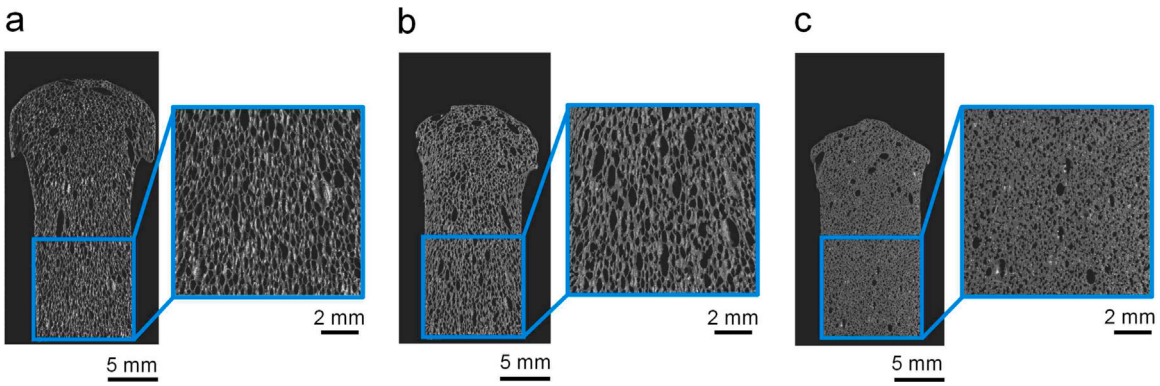

Fig. 1. Optical micrographs of the vertical cross-sections of *h*-MRE foam samples with increasing particle content: (a) 70 phr (c_v = 0.606, c_p = 0.032), (b) 140 phr (c_v = 0.593, c_p = 0.062), and (c) 210 phr (c_v = 0.413, c_p = 0.124). Each inset corresponds to the 10 mm × 10 mm zone of interest.

Table 2
Volume fraction of voids c_v, and volume fraction of particles in the matrix c_{pm} and in the foam sample c_p, estimated from 10 different samples.

phr	c_v	c_{pm}	c_p
70	0.612 ± 0.020	0.082 ± 0.000	0.032 ± 0.002
140	0.594 ± 0.011	0.151 ± 0.000	0.061 ± 0.002
210	0.418 ± 0.050	0.211 ± 0.001	0.123 ± 0.011

ρ_s = 1,021 kg/m^3 and is obtained experimentally by weight measurements of known volumes of fluid components, while ρ_p = 7,640 kg/m^3 and is provided by the manufacturer. The mass M_f and volume V_f of the samples are measured after fabrication thus providing ρ_f.

Next, the volume fraction of particles in the *h*-MRE matrix, c_{pm}, is estimated as

$$c_{pm} = \frac{V_p}{V_p + V_s} = \frac{\rho_s M_p}{\rho_p M_s + \rho_s M_p} = \frac{\rho_s\, phr}{\rho_s\, phr + 105\,\rho_p}. \tag{5}$$

Here, we clarify that the $V_p + V_s$ denotes the volume of the pure *h*-MRE matrix without the voids, and that particles remain confined to the matrix, thus being absent in the voids.

Then, the volume fraction of the particles in the entire foam sample c_p is simply evaluated as a function of c_{pm} and c_v from the relation

$$c_p = \frac{V_p}{V_f} = \frac{V_p}{V_p + V_s}\,\frac{V_p + V_s}{V_f} = c_{pm}\,(1 - c_v). \tag{6}$$

Based on the above equations, the values of porosity and particle filling factors obtained for the 10 different samples corresponding to 70, 140 and 210 phr are reported in Table 2. These results exhibit minimal dispersion but more importantly demonstrate unambiguously that the increase of particle filling factor in the silicon matrix c_{pm} leads to a decrease of the resulting porosity c_v during the foaming process. The total particle volume fraction c_p instead increases similarly to c_{pm}. The particle content thus significantly influences the generation of voids in the *h*-MRE foam, as also noticed in polyurethane foams [40]. This may be intuitively explained by noting that as the particle content increases, the pure *h*-MRE matrix becomes heavier [50] and thus hinders the growth of the bubbles generated by the foaming agent.

3.2. Voids shape and size characterization

Optical microscope images of the vertical cross-sections of *h*-MRE foams of 70, 140 and 210 phr are presented in Fig. 1 while horizontal cross-sections, obtained on another series of samples, are reported in Fig. 2. The structure of the foam comprises an *h*-MRE composite matrix and closed-cell pores. In the vertical cross-sections (Fig. 1), the pores appear aligned along the foaming direction and exhibit roughly an elliptical shape, with their ellipticity decreasing with the increase of phr. In contrast, in the horizontal cross-sections (Fig. 2), the pores exhibit a more circular shape and moderate dispersion in size. Hence, overall the pores are ellipsoidal (with almost circular cross-section in the horizontal plane), and as the content of particles increases from 70 to 210 phr, both the size and aspect ratio of the pores decrease, indicating smaller and less elongated voids with higher phr.

Since the size and shape distributions of voids have an important effect on the properties of foams, be they mechanical or acoustic [51,52], quantitatively assessing the size and shape distribution of the voids in the foam samples appears of interest for gaining insight into the microstructure–properties relationship. For this purpose, Python-based image processing of cross-sectional micrographs is carried out as detailed in Appendix B. We identify first the boundaries of the voids, and then use ellipse fitting to determine their size and shape in the given cross-section. Subsequently, the characteristics of the detected ellipses are analyzed quantitatively to serve as input in the next section.

3.3. Virtual microstructure reconstruction

The goal here is to reconstruct numerically the microstructural features of the voids obtained experimentally. Given the ellipsoidal geometry of the voids, we employ the random sequential adsorption (RSA) method developed by Anoukou et al. [53] to reconstruct periodic, representative volume elements (RVEs) that have the same shape statistics as the fabricated samples. The periodicity of the cells, as discussed in detail in Section 5, allows to analyze numerically the magnetic response of the material considering substantially smaller volumes than the actual sample volume [54]. This method extends the well-known RSA approach [55,56] to create non-overlapping random mono- and polydisperse ellipsoidal inclusions of any shape, orientation and size. The details of the algorithm are not repeated here for brevity.

We observe in Fig. 3 that the aspect ratio of the ellipsoidal voids in the real foam follows a Gaussian-type distribution in the vertical direction (see red line). In this regard, the RSA algorithm of Anoukou et al. [53] is modified to generate microstructures with a random Gaussian-type aspect ratio specified as input. We remark that post-processing of the numerical microstructure delivers the same distribution than the input one (red line in the figure) and thus is not shown for clarity. In the horizontal direction, we set the aspect ratio of the voids equal to unity for simplicity. It has been shown in Zerhouni et al. [57], in the context of elasticity (which is not different from the case of magnetism), that for randomly oriented ellipsoidal voids, the material response is only weakly affected by the aspect ratio for values less than 2. Fig. 3a–c compares the numerical and real foam aspect ratios, while the bottom part of the figures illustrates cubic RVEs as created with the RSA method (the voids are in gray).

It is important to note that the aim of the numerical reconstruction is not to replicate the exact number of voids, since the real foam contains thousands of voids in a given specimen, but to generate a

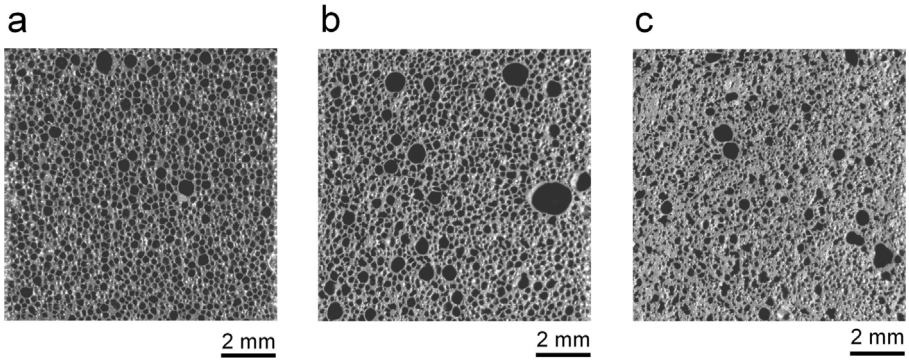

Fig. 2. Optical micrographs of the horizontal cross-sections of *h*-MRE foam samples with increasing particle content: (a) 70 phr (c_v = 0.606, c_p = 0.032), (b) 140 phr (c_v = 0.593, c_p = 0.062), and (c) 210 phr (c_v = 0.413, c_p = 0.124).

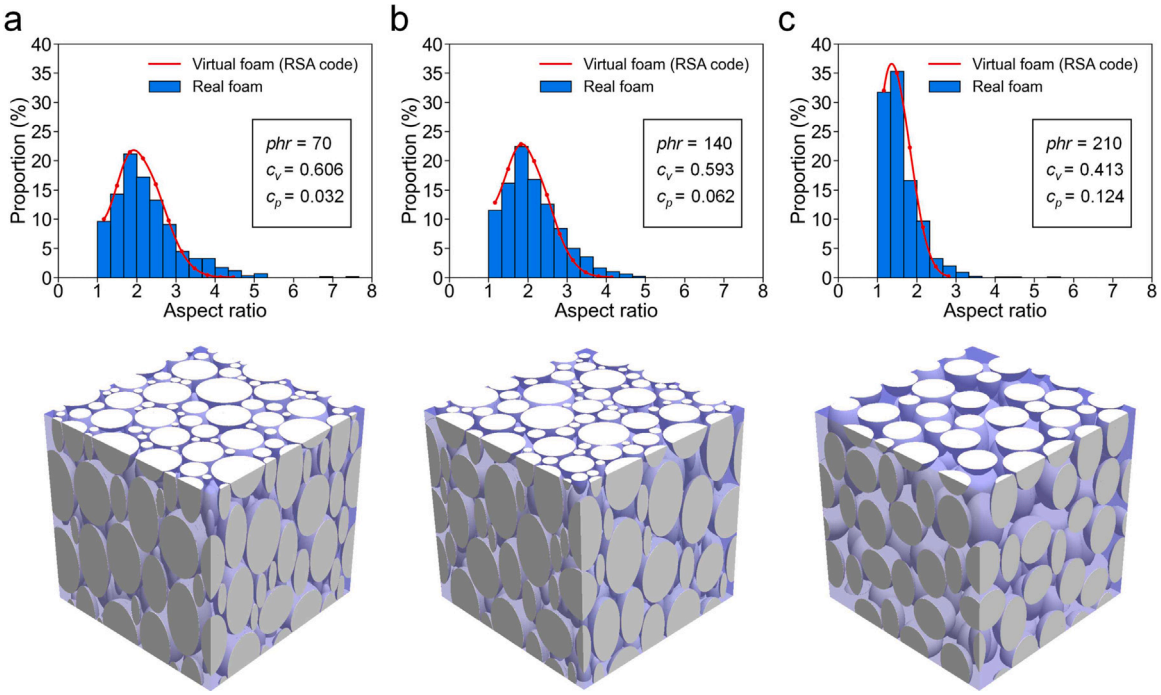

Fig. 3. Comparison of the void shape characteristics of virtually generated microstructures of *h*-MRE foams with those of the real foam. The results show the aspect ratio distribution in the vertical direction. The *h*-MRE foams contain varying particle and void contents identical to the measurements: (a) 70 phr (c_v = 0.606, c_p = 0.032) containing 592 voids, (b) 140 phr (c_v = 0.593, c_p = 0.062) containing 562 voids and (c) 210 phr (c_v = 0.413, c_p = 0.124) containing 204 voids.

sufficient number of voids with the same *statistical* characteristics as the real foam that can deliver a representative response under periodic boundary conditions [17,58]. We close by noticing that the porosity of the foams is less than 61%, which allows us to use the RSA polydisperse approach of Anoukou et al. [53]. For larger porosities, however, it becomes increasingly difficult to place new non-overlapping voids [59] and in such cases, one may resort to other available methods such as those proposed by Hooshmand-Ahoor et al. [60,61].

4. Magnetic characterization of *h*-MRE foam samples

4.1. Magnetization process and remanent magnetization measurements

The *h*-MRE foam samples are exposed to a strong external magnetic field, denoted as $\mathbf{h}^{\text{app}}$, resulting in the development of a remanent magnetic field, denoted as $\mathbf{b}^r$ upon removal of $\mathbf{h}^{\text{app}}$. This magnetization process is carried out using a two-coil electromagnet (Bouhnik, France) equipped with iron poles of 20 mm diameter separated by an air gap of 10 mm (see sketch in Fig. 4a), such that the field is uniform (< 1% deviation) where the sample is installed within the gap. Irrespective of minor magnetic field non-uniformities that may be present, of essence in the present process is to reach magnetization saturation everywhere in the sample and thus uniform magnetization upon removal of the applied magnetic field. This is achieved by applying a sufficiently large field as will be discussed below in the context of Fig. 6.

The samples are installed between the poles using a 3D-printed insert (a disk of 20 mm diameter and 10 mm height with a square through-hole at its center), so that their top and bottom sides are centered and in contact with the poles. During magnetization, we increase the magnetic field from 0 to 3.1 T and then decrease it back to 0 T at a controlled rate. The foam samples are positioned in two distinct orientations with respect to the applied magnetic field $\mathbf{h}^{\text{app}}$. The first one places the major axis of the ellipsoidal voids, whose orientation is denoted as $\mathbf{n}$ for clarity, aligned with the applied magnetic field, i.e., $\mathbf{h}^{\text{app}} \parallel \mathbf{n}$ (Fig. 4b). In the second case, the major axis of the ellipsoids is perpendicular to the applied magnetic field, i.e., $\mathbf{h}^{\text{app}} \perp \mathbf{n}$ (Fig. 4c).

Upon removal of the externally applied magnetic field $\mathbf{h}^{\text{app}}$, we proceed to the measurement of the magnetic properties of the foam, which

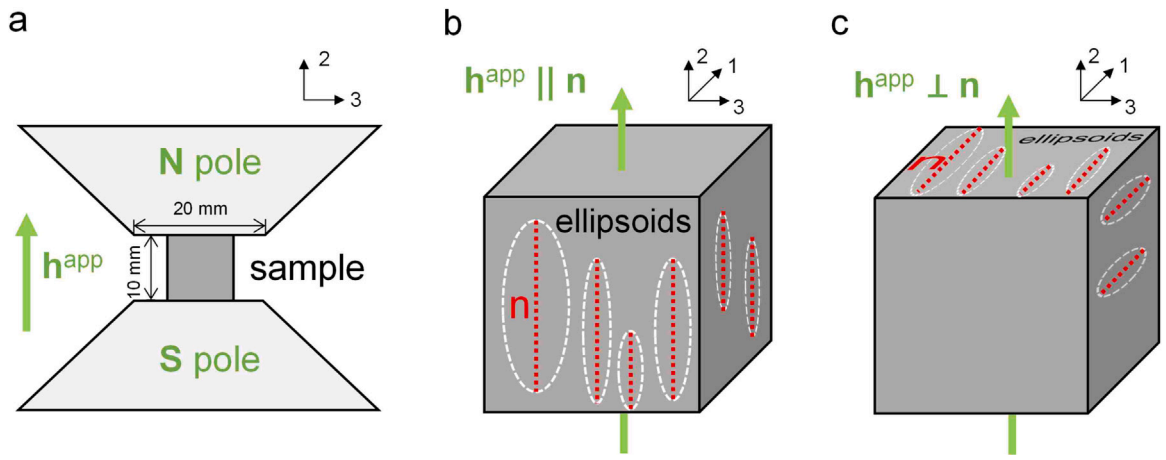

Fig. 4. Magnetization of *h*-MRE foam samples denoting as $\mathbf{h}^{app}$ the applied magnetic field and **n** the orientation of the major axis of the ellipsoidal voids. (a) Sketch of the sample positioning between the electromagnet poles during magnetization. (b) $\mathbf{h}^{app} \parallel \mathbf{n}$ magnetization configuration, and (c) $\mathbf{h}^{app} \perp \mathbf{n}$ magnetization configuration.

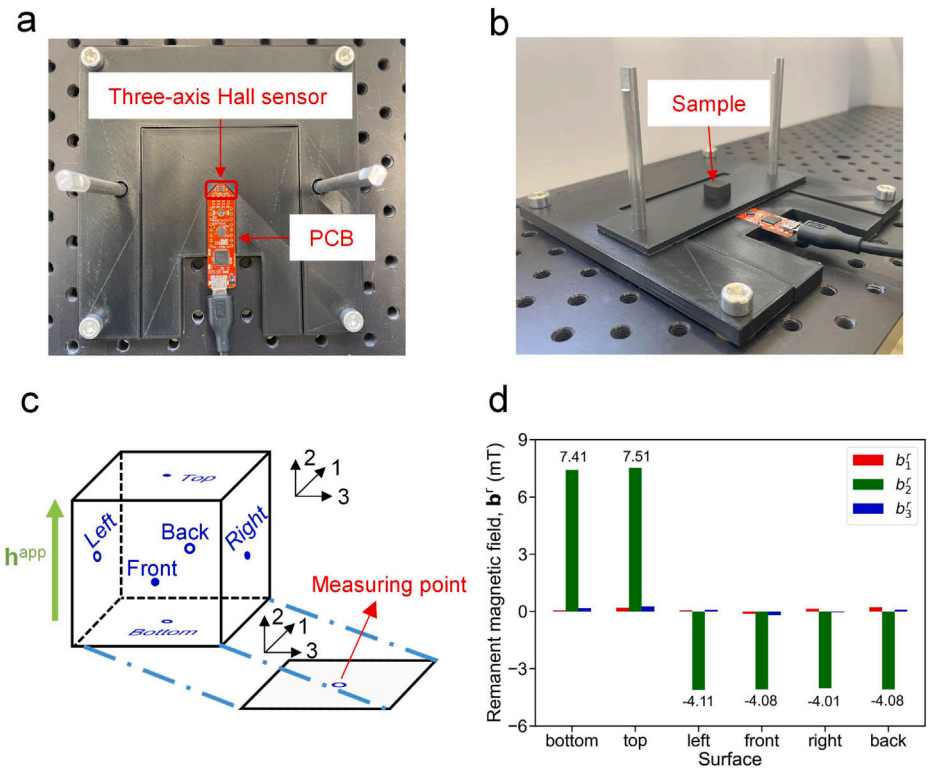

Fig. 5. Remanent magnetic field measurements on *h*-MRE foam samples. (a) PCB with three-axis Hall sensor installed within a 3D-printed support, (b) 3D-printed centering template used to place the center of the probed face of the cubic sample in contact with the sensor, (c) sketch of measurement locations and orientations, and (d) example of measurement obtained on a 70 phr sample magnetized in the $\mathbf{h}^{app} \parallel \mathbf{n}$ configuration.

now acts as a permanent magnet due to the remanent magnetization induced by the magnetized particles in the polymer phase.

The remanent magnetic field $\mathbf{b}^r$ is measured with a TLE493D-W2B6 MS2GO three-axis Hall sensor (Infineon Technologies, Germany) integrated into a printed circuit board (PCB), and having a range of ± 160 mT with a resolution of 130 μT. The PCB is installed inside a 3D printed support base to maintain it horizontal (see Fig. 5a). We use a 3D-printed centering template to place the cubic samples so that the center of the probed *h*-MRE foam face is in contact with the sensor (see Fig. 5b). By convention, irrespective of the ellipsoid orientation during magnetization, the bottom and top faces correspond to the faces that were in contact with the south and north poles respectively, as indicated in Fig. 5c. At each measurement point, all three components of remanent magnetic field b_1^r, b_2^r and b_3^r are recorded (Fig. 5d).

As expected (and will be further confirmed in Section 5), the maximum component of the remanent magnetic field is measured along the magnetization direction (b_2^r) at the top and bottom faces that were in contact with the poles of the electromagnet. For these faces, the b_1^r and b_3^r contributions are nearly zero. On all other faces (front, back, left and right), which are equivalent with respect to the magnetization direction, the largest component of the remanent magnetic field is also along the magnetization direction (b_2^r) but of opposite sign and of smaller amplitude (with values within 6% of the average), while the other components b_1^r and b_3^r are again nearly zero. Henceforth, in the remaining of the study, we focus on the average maximum remanent field b_2^r, as measured at the top and bottom faces of the sample that were in contact with the electromagnet's poles.

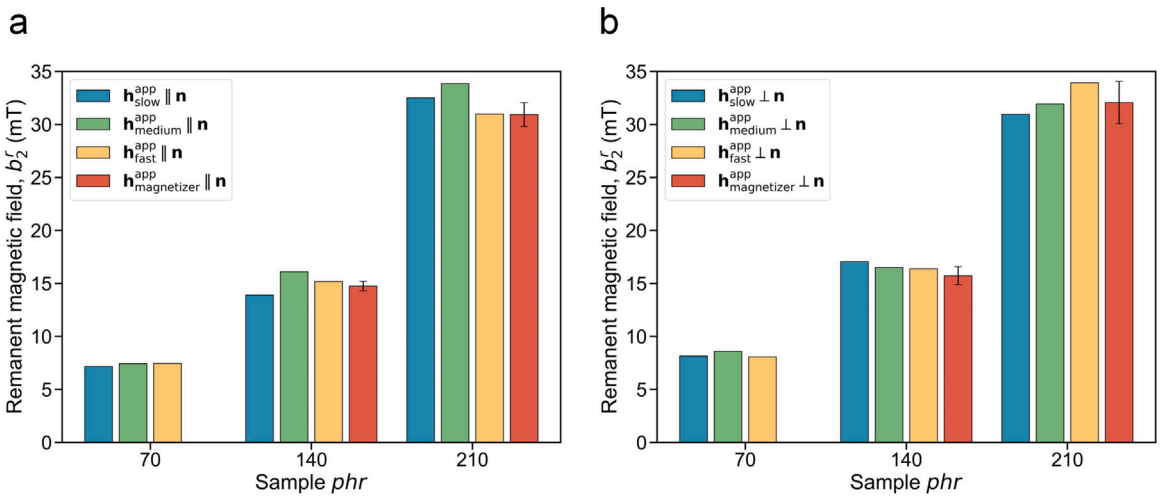

Fig. 6. Remanent magnetic field measured on samples of different particle contents magnetized at different magnetic speeds (a) in the $\mathbf{h}^{app} \parallel \mathbf{n}$ configuration, and (b) in the $\mathbf{h}^{app} \perp \mathbf{n}$ configuration.

4.2. Influence of magnetization speed

In order to assess the influence of the magnetization speed on the remanent magnetic field of the *h*-MRE foam samples, we magnetize samples of different particle contents with the speed of magnetization spanning three decades: 4.34×10^{-3} T/s ("slow"), 4.34×10^{-2} T/s ("medium"), and 4.34×10^{-1} T/s ("fast"). Fig. 6a shows results for samples magnetized in the $\mathbf{h}^{app} \parallel \mathbf{n}$ configuration and Fig. 6b for samples magnetized in the $\mathbf{h}^{app} \perp \mathbf{n}$ configuration.

For the sake of completeness, we also include data for samples of 140 and 210 phr that are magnetized using an impulse magnetizer (DXMM-12C40 Magnetizer, Dexing Magnet Tech. Co., Limited, China) capable of delivering a field above 5 T at the center of a 50 mm coil in 2 s (see [62]). For each particle content, three samples are magnetized in both the $\mathbf{h}^{app} \parallel \mathbf{n}$ and $\mathbf{h}^{app} \perp \mathbf{n}$ configurations, and results are indicated in Fig. 6 with the label "$\mathbf{h}^{app}_{magnetizer}$". The error bars correspond to two standard deviations stemming from the measurements made on three different samples for each case.

Within the range of speeds considered here, we observe no appreciable effect of the magnetization speed upon the measured remanent magnetic field of *h*-MRE foam samples, regardless of their particle content or magnetization direction. Therefore, it can be concluded that the remanent magnetic field in the *h*-MRE foam samples is independent of the speed of magnetization as long as it is above the nominal remanent flux of the magnetic powder. In the remaining of the study, all results correspond to samples magnetized inside the electromagnet at medium speed.

4.3. Influence of sample microstructure

In this section, we investigate the effect of the sample microstructure on the remanent magnetic field $\mathbf{b}^r$. For each considered particle content, three samples are magnetized in the $\mathbf{h}^{app} \parallel \mathbf{n}$ and $\mathbf{h}^{app} \perp \mathbf{n}$ configurations, and average results of the b_2^r component of the remanent magnetic flux are reported in Fig. 7 with the error bars corresponding to the standard deviation.

Fig. 7a shows that the orientation of the voids (i.e., ellipsoids filled with air) during the magnetization process does not affect the remanent magnetic field exhibited by the samples after magnetization. Hence, *h*-MRE foam magnetization is independent of the morphological anisotropy of the voids. This is not intuitive but can be explained by the fact that the voids have the same exact magnetic permeability than that of the matrix and the vacuum. As a consequence, the anisotropically porous foam can simply be considered as continuum permanent magnet with uniform magnetization, which is of importance when it comes to modeling its magnetic behavior numerically. This point is discussed in more detail in the numerical analysis Section 5.2. The results in Fig. 7a also imply that the particles are fairly uniformly distributed in the intervoid ligaments, and no additional microscopic anisotropy is present. Furthermore, as clearly illustrated in Fig. 7b, the only parameter that appears to influence the remanent magnetic field is the particle content and, in particular, we observe a linear dependence of b_2^r on the particle volume fraction c_p. Despite the approximations employed to estimate c_p in Section 3.1, the linearity between b_2^r and c_p seems to be a fundamental property of the present *h*-MRE foams. This linearity will be confirmed rigorously via full field numerical simulations of the RVE and the sample in the following section.

5. Theoretical and numerical modeling of the magnetic behavior

In Section 4.3, we have shown experimentally that the remanent magnetic flux at the middle point of the top (and bottom) surface of the sample is independent of the morphology of the voids within the foam. Herein, we establish a general modeling approach allowing to probe this response everywhere in the sample and predict the response for arbitrary porosities, particle volume fractions and sample geometries.

This analysis is done in two steps. First, a 3D numerical model of a representative volume element (RVE) of an *h*-MRE foam is generated using the statistically relevant microstructures discussed in Section 3.3 in order to properly assess the influence of void shape orientation as well as of particle volume fraction on the magnetic response. Then, the homogenized *h*-MRE model for the foam is implemented and resolved numerically for a cube embedded in air (BVP).

5.1. The general magnetic model valid for h-MRE materials with or without voids

In this work, we adopt the homogenization-guided continuum model proposed by Mukherjee et al. [17] to describe the response of both the *h*-MRE composite matrix and the *h*-MRE foam, which exist naturally in two different scales. The *h*-MRE matrix is a composite material made of a silicon matrix and micron-sized particles, and thus the model of Mukherjee et al. [17] may be used as such. Instead, the *h*-MRE foam has a third phase, that of the voids, but at a larger scale. In this case, we will show that the same Mukherjee et al. [17] model for the magnetic response only may be used by recalling the "homogenized" expression (6) for c_p. Specifically, if one sets $c_v = 0$ in (6) then a bulk *h*-MRE material is obtained. Instead, when $c_v \neq 0$, we will show that the same

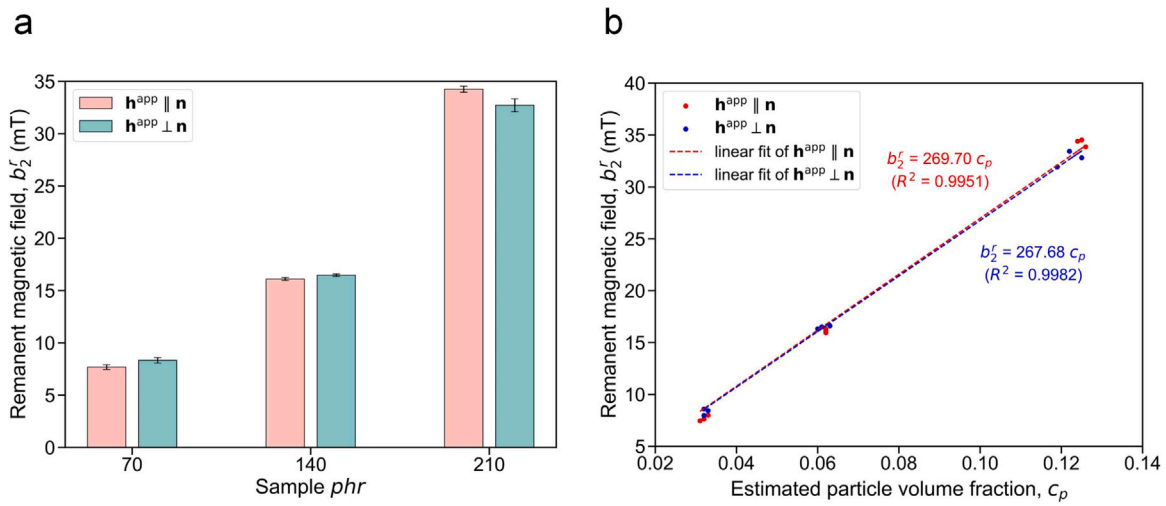

Fig. 7. Remanent magnetic field b_2^r measured in samples of different particle contents magnetized at medium speed in the $\mathbf{h}^{app} \parallel \mathbf{n}$ and in the $\mathbf{h}^{app} \perp \mathbf{n}$ configurations as a function of (a) phr, and (b) c_p.

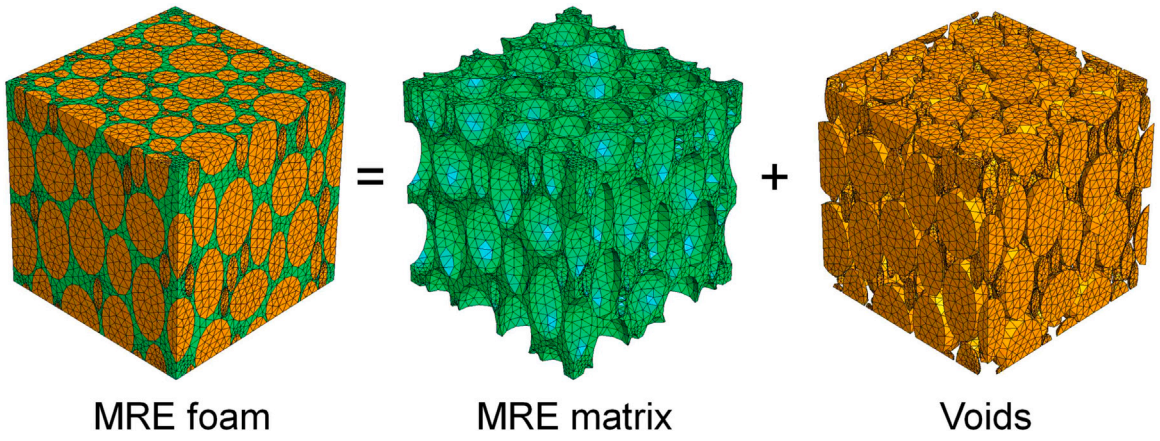

Fig. 8. The microstructure and mesh used for RVE simulations. The MRE foam consists of an MRE matrix and voids. The void phase is meshed to represent air, facilitating the transfer of the magnetic field.

expression for c_p can be used to deliver accurate results for the *h*-MRE foam.

Before we proceed to specific results, we recall briefly from Mukherjee et al. [17], the relevant magnetic energy density and dissipation potential used in the present study to estimate the magnetic properties of the *h*-MRE matrix and foam. Note that the energy density and dissipation potential do not include at this stage any mechanical or magneto-mechanical coupling term since the samples did not exhibit a measurable change in their dimensions after magnetization and are not subjected to any additional mechanical loading in the present study. We consider that the particles are distributed uniformly and isotropically in the silicon and thus we assume that the response of the *h*-MRE matrix is magnetically isotropic, as also justified by the experimental results in Fig. 7. A straightforward and elegant way to satisfy the conditions of isotropic material symmetry and frame indifference is to express the energy density and dissipation in terms of properly chosen *isotropic* invariants, such as

$$I_5^{\mathrm{h}} = \mathbf{h} \cdot \mathbf{h}, \qquad I_5^{\mathrm{hhr}} = \mathbf{h} \cdot \boldsymbol{\mathcal{H}}^r, \qquad I_5^{\mathrm{hr}} = \boldsymbol{\mathcal{H}}^r \cdot \boldsymbol{\mathcal{H}}^r. \tag{7}$$

In these definitions, $\mathbf{h}$ is the magnetic field strength or *h*-field, while $\boldsymbol{\mathcal{H}}^r$ is a remanent field of similar units that acts as an internal variable and is responsible for the resulting dissipation of the magnet. Note that the $\boldsymbol{\mathcal{H}}^r$ will not be exactly the same than $\mathbf{h}^r$, which is the remanent *h*-field after the removal of the externally applied magnetic field.

The pure magnetic free energy is expressed in terms of these I_5-based invariants, such that

$$W_{\mathrm{mag}}(\mathbf{h}, \mathbf{h}^r) = -\frac{\mu_0}{2}\chi^e I_5^{\mathrm{h}} + \mu_0(1+\chi^e) I_5^{\mathrm{hhr}} + \frac{\mu_0}{2}\left(\frac{1-c_p}{3c_p}\right) I_5^{\mathrm{hr}} + \frac{\mu_0}{c_p}\frac{(m^s)^2}{\chi_p^r} f_p\left(\frac{\sqrt{I_5^{\mathrm{hr}}}}{m^s}\right), \tag{8}$$

which leads to the magnetic constitutive behavior

$$\mathbf{b}(\mathbf{h}, \mathbf{h}^r) = \frac{\partial W_{\mathrm{mag}}}{\partial \mathbf{h}}. \tag{9}$$

Here χ_p^r is the *remanent susceptibility* of the underlying magnetic particle, whereas the "effective" parameters χ^e and m^s for the composite are given in terms of the particle magnetic properties and its total volume fraction c_p (see (6)) as

$$\chi^e = \frac{3c_p\chi_p^e}{3+(1-c_p)\chi_p^e}, \qquad m^s = c_p\, m_p^s\left(\frac{1+\chi_p^e}{1+\chi^e}\right), \tag{10}$$

where χ_p^e and m_p^s are the particle *energetic susceptibility* and *saturation magnetization*.[2] Moreover, $f_p(x)$ is a nonlinear function that leads to a

[2] A graphic explanation of these parameters is provided in Fig. 2 of Mukherjee et al. [17] and is not repeated here for brevity, whereas the reader is also

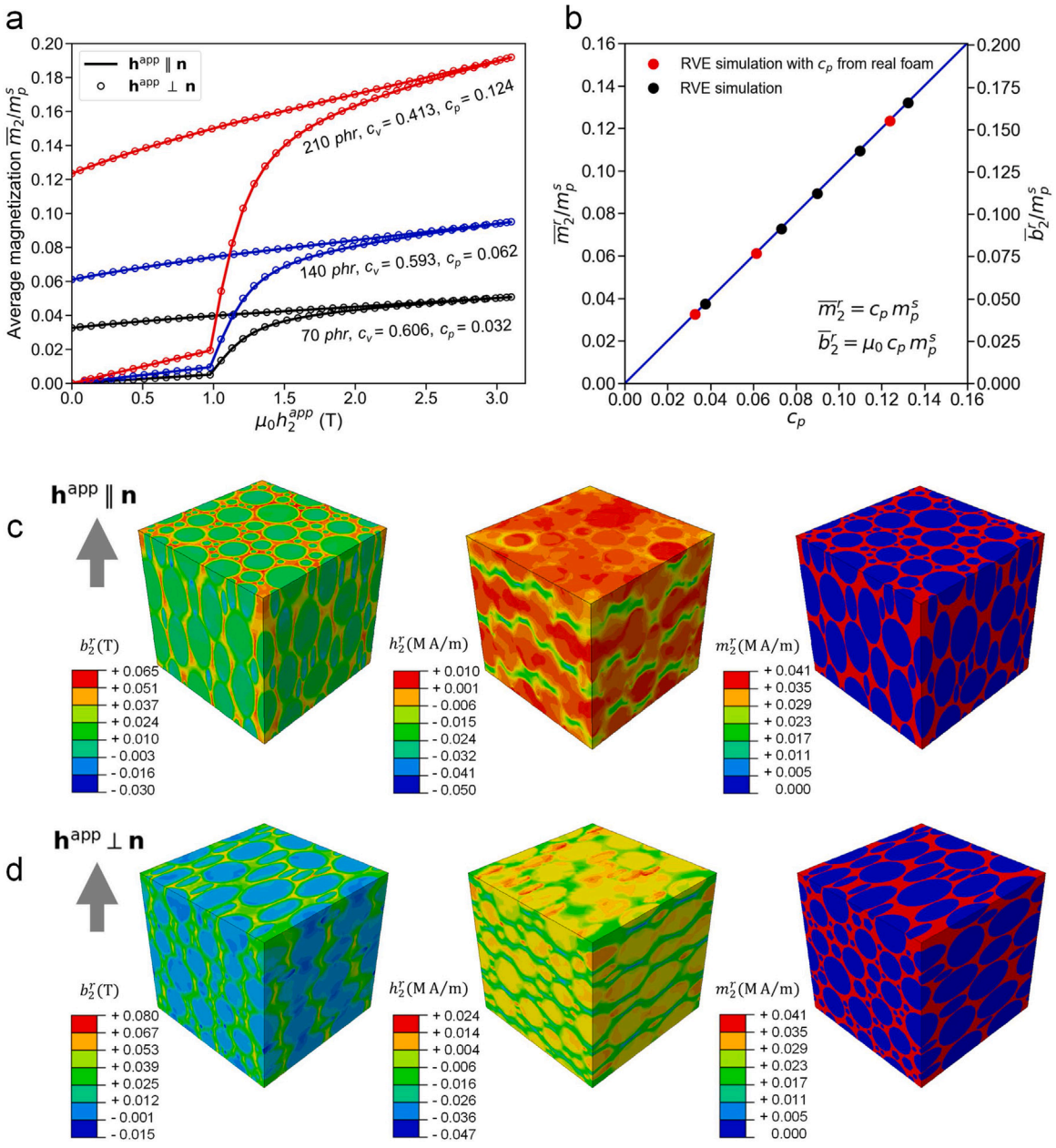

Fig. 9. Results of the RVE simulations of *h*-MRE foams. (a) Normalized magnetization of three different foams (corresponding to those experimentally studied), magnetized in parallel and perpendicular orientations. (b) Average normalized remanent fields $\overline{m}_2^r/m_p^s$ and $\overline{b}_2^r/m_p^s$ as a function of particle volume fraction c_p. (c) Contours of b_2^r, h_2^r and m_2^r remanent fields of the foam with 70 phr (c_v = 0.606, c_p = 0.032), under h-field applied parallel and (d) perpendicular to the major axis **n**.

saturation-type magnetization behavior, such as the inverse hypergeometric function used here, which reads

$$f_p(x) = -[\log(1-x) + x]. \tag{11}$$

Next, we define a rate-independent dissipation potential, D, terms of $\dot{\boldsymbol{\mathcal{H}}}^r$ only, such that [17,48]

$$D(\dot{\boldsymbol{\mathcal{H}}}^r) = b^c\, |\dot{\boldsymbol{\mathcal{H}}}^r| \geq 0, \tag{12}$$

where $|.|$ denotes the standard Eulerian norm and b^c is the effective *coercive field* of the composite given by

$$b^c = b_p^c \left(\frac{1+\chi^e}{1+\chi_p^e} \right)^{4/5}. \tag{13}$$

In this expression, b_p^c and χ_p^e are the particle coercivity and energetic susceptibility, respectively, whereas χ^e has been defined in Eq. (10). Typically, for a hard-magnetic composite, the effective coercivity is given by $b^c = b_p^c$ [63]. Nonetheless, the multiplicative term of b_p^c in Eq. (13) serves as an effective correction term for an actual magnet and can be obtained from available experimental data [48].

After some mathematical manipulation described in Mukherjee et al. [17], we obtain a criterion known as *ferromagnetic switching*

referred to Mukherjee and Danas [48] for a more complete study of magnetic response.

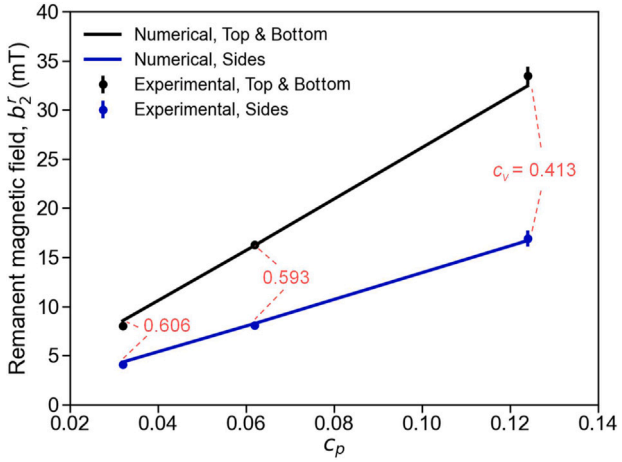

Fig. 10. The results of the numerical BVP solved with m_p^s= 0.51 MA/m, compared with experimental measurements at the top, bottom, and side faces.

surface, which reads [48,65]

$$\Phi(\mathcal{B}^r) := |\mathcal{B}^r|^2 - (b^c)^2 = 0. \tag{14}$$

In this last expression, $\mathcal{B}^r$ is a remanent magnetic flux-like vector field conjugate to $\mathcal{H}^r$ but is not equal to the remanent $\mathbf{b}^r$ field of interest in the present work. This last criterion (similar to the yield surface in J_2 flow theory of elasto-plasticity) must be satisfied during a magnetic loading/unloading cycle. The evolution of $\mathcal{H}^r$ is then obtained by using the normality rule to the switching surface, such that

$$\dot{\mathcal{H}}^r = \dot{\Lambda}\frac{\partial \Phi}{\partial \mathcal{B}^r}, \qquad \Phi(\mathcal{B}^r) \le 0, \qquad \dot{\Lambda} \ge 0 \qquad \text{and} \qquad \dot{\Lambda}\Phi = 0, \tag{15}$$

with $\mathcal{H}^r(t = 0) = \mathbf{0}$. These conditions are also known as the Karush–Kuhn–Tucker (KKT) conditions [66,67].

With Eq. (15), the evolution equations for the internal vector variable $\mathcal{H}^r$ are now fully defined. Evidently, this model is path- and history-dependent. Its mathematical similarity to J_2 flow theory of plasticity allows us to resort to already well-known numerical algorithms (such as the radial return algorithm) to resolve the evolution equations and evaluate the deformation and magnetic fields under general magnetic loads. The model must be solved numerically, as is the case in all incremental elasto-plastic models in the literature. Numerical implementations of the model in user element routines for ABAQUS [68] and FEniCS are available in Mukherjee et al. [69] and Rambausek et al. [70], respectively. In the present study, we use the implementations in Abaqus.

5.2. Microstructural RVE simulations

We investigate the effect of ellipsoidal voids orientation on the magnetic properties of the *h*-MRE foam by conducting a 3D full-field representative volume element (RVE) simulation on the virtual foam microstructures obtained in Section 3.3. This corresponds to an analysis of a two-phase material comprising the voids (in the order of 50–100 μm) and an *h*-MRE composite matrix which is free of voids and carries the magnetic particles. The particles, which are much smaller than the voids (i.e., in the order of 5 μm), are taken into account by the homogenized model presented in the previous section by setting $c_v = 0$ in all expressions such that $c_p = c_{pm}$. With this analysis, we aim at showing rigorously that the *average* remanent magnetic field $\mathbf{b}^r$ in the foam material and at its surface scales linearly with the particle volume fraction everywhere in the sample, which further supports the experimental observations in Fig. 7b.

A conformal mesh composed of ten-node, quadratic tetrahedral elements (C3D10) is generated using the open-source mesh generation software GMSH. Fig. 8 illustrates an example of the mesh created for the microstructure with c_v = 0.606 and c_p = 0.032 (70 phr), as introduced in Fig. 3a. We remark that the void phase needs to be meshed in order to allow for the proper continuity of the magnetic fields everywhere in the sample.

Table 3
Magnetic properties of the NdFeB particles.

χ_p^e	χ_p^r	b_p^c (T)	μ_0 (μN · A^2)
0.105	8.0	1.062	$4\pi 10^{-1}$

We also apply periodic boundary conditions across opposite boundaries of the RVE following the methodology established by Danas [58] in two dimensions and extended in three dimensions in Mukherjee et al. [17] and Mukherjee and Danas [18] (and not repeated here for brevity).

In the experiments proposed in this study, we have information on the remanent magnetic field $\mathbf{b}^r$ but not the entire history of $\mathbf{b}$. In the context of the present complete model presented in the previous section, it is necessary, however, to provide values for all relevant material parameters. Following earlier studies, we choose those parameters as reported in Table 3. It is noted that those parameters do not affect the final distribution of the magnetic fields in the sample upon removal of the magnetic field, provided that the sample is magnetized sufficiently to reach the magnetization saturation regime, where no more magnetic dissipation is expended.

In contrast, we allow the *scalar* magnetization saturation of the particles m_p^s to serve as the calibration parameter of the model. For this reason, in the RVE simulations, we show all results normalized with that material property. Its precise value will be identified in Section 5.3 by use of experimental data.

An average magnetic field b_2^{app} is applied in the RVE, which is increased from 0 to 3.1 T, and decreased back to 0 T. As shown in Section 4.2, the magnetization process is rate-independent as is the model presented here and thus the rate of application of b_2^{app} is inconsequential. The microstructure can be oriented such that the major axis of the voids is parallel or perpendicular to the average applied field b_2^{app}. A single RVE realization takes approximately three hours to run for a mesh with approximately 300,000 degrees of freedom using 40 cores in parallel.

Fig. 9a shows the average normalized magnetization $\overline{m}_2/m_p^s$ in the RVE for three different foams (corresponding to those experimentally studied) magnetized in parallel and perpendicular orientations with respect to the major axes of the voids. At fixed particle volume fraction c_p, the magnetization response is independent of the magnetization direction. Furthermore, increasing the particle content results in higher magnetization, particularly in terms of remanent magnetization. Additional RVE simulations are conducted on microstructures with different particle volume fractions c_p than those studied experimentally. Fig. 9b shows the average normalized remanent fields $\overline{m}_2^r/m_p^s$ (left *y*-axis) and $\overline{b}_2^r/m_p^s$ (right *y*-axis) as a function of particle volume fraction c_p, where m_p^s is the saturation magnetization of the particles, whose exact value for the present materials will be determined in the next section. The red markers correspond to RVE simulations on virtually reconstructed microstructures from experimental data with identical c_p. It can be observed that both $\overline{b}_2^r$ and $\overline{m}_2^r$ exhibit a linear relation with respect to the particle volume fraction c_p such that $\overline{m}_2^r = c_p m_p^s$ and $\overline{b}_2^r = \mu_0 c_p m_p^s$.

Fig. 9c and d illustrate contours of local b_2^r, h_2^r and m_2^r remanent fields for c_v = 0.606 and c_p = 0.032 (70 phr) foam, under applied field parallel and perpendicular to the major axis of the ellipsoids, respectively. Interestingly, despite significant variations in b_2^r and h_2^r between the two cases, m_2^r remains unchanged whether the $\mathbf{h}$ field is applied parallel or perpendicular to the major axis $\mathbf{n}$. Furthermore, m_2^r remains uniform throughout the matrix, regardless of the complexity and differences in local b_2^r and h_2^r. This may be simply explained by noting that the magnetic permeability is equal to μ_0, as is the case in

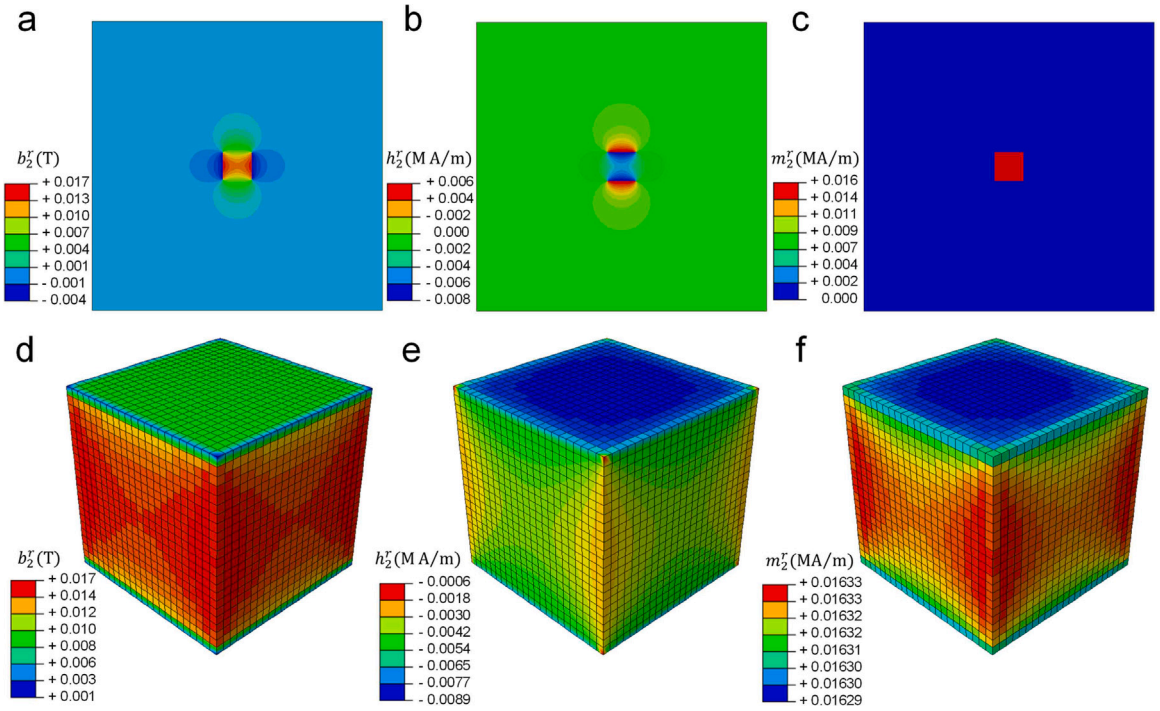

Fig. 11. The contours of b_2^r, h_2^r and m_2^r remanent fields of the foam with c_v = 0.606 and c_p = 0.032 (70 phr) (a)–(c) in a cross-section of air and foam domains, (d)–(f) inside the uniform h-MRE foam cube sample.

the silicon matrix and thus these two otherwise different components (silicon and air) behave in the same fashion when it comes to magnetic properties. What is interesting, however, is that the elongated geometry of the voids and thus the concentration of the particles in oriented matrix domains does not affect the magnetization response which remains overall "isotropic". This important observation allows to construct next a very simple approach for the h-MRE foam.

5.3. Macroscopic boundary value problem (BVP) of h-MRE foams and constitutive relations

Starting from the previous observation of linearity between the remanent fields and the particle volume fraction, one may directly use the exact same model described in Section 5.1 for the h-MRE foam this time. We only need to identify the particle volume fraction c_p with that in the entire foam, i.e., as defined in Eq. (6) setting c_{pm} equal to the volume fraction in the h-MRE matrix phase and c_v equal to the void volume fraction in the foam.

This simple but powerful result allows to scale up our analysis to the sample size and solve numerically the entire boundary value problem (BVP) with realistic boundary conditions. In addition, using the solution of the BVP, one obtains a value for the magnetization saturation of the particles m_p^s and can compare directly with the experimental data.

In Fig. C.17, we show the geometry and mesh of the analyzed BVP. We consider a cube of dimensions L^3 embedded in a large air domain ($(10L)^3$). A far-field magnetic field b_{app} with maximum value 3.1 T is applied to bring the cube to magnetic saturation and then is removed. We use hexahedral bilinear eight-node isoparametric elements (C3D8) to analyze the problem. Fine meshing is required near the corners to capture accurately the strong magnetic field gradients. For the magnetic problem, we use a scalar potential approach as the one described in Mukherjee et al. [17].

The BVP is used to identify the remaining material parameter m_p^s, which corresponds to the magnetization saturation of the particles. Note that the experimental magnetic measurements are conducted after magnetization, i.e., only the remanent fields are measured at fixed locations. For this reason, we assume the magnetic properties of the particles to be the same than those used in the RVE simulations and correspond to Table 3 of Mukherjee et al. [17].

Specifically, we use the experimental remanent flux b_2^r for the 140 phr h-MRE foam, corresponding to c_p = 0.061 (see Table 2) to solve the boundary value problem. The remanent field b_2^r is estimated at the center of both the bottom and top surfaces, as in the experiment. We find that a value m_p^s = 0.51 MA/m gives the best fit between the experiments and the numerical remanent flux b_2^r. This value is then used in Fig. 10 to simulate different particle and void volume fractions c_p and c_v, respectively. We observe an excellent agreement between the model predictions and the experimental measurements for all cases considered.

For completeness, we show in Fig. 11 corresponding contours at a cross-section of the entire domain (a–c) as well as for the cubic h-MRE foam (d–f). In Fig. 11a and b the remanent b_2^r and h_2^r appear highly heterogeneous. In contrast, the remanent magnetization m_2^r in Fig. 11c may be considered practically uniform in the cube since the heterogeneity computed appears in the fourth digit (i.e., in the order of a few hundreds of A.m).

This observation reveals that irrespective of the non-uniformities inherent in the magnetic flux b and magnetic field strength h, their contributions to the magnetization $m = b/\mu_0 - h$ remain constant. Finally, the effect of sample geometry on the distribution of the magnetic remanent fields and resulting magnetization is studied in Appendix C.

5.4. A simple analytical solution for the remanent magnetic flux of parallelepiped geometries

Following the Biot–Savart law and a magnetic vector potential formalism, Gou et al. [64] derived analytical expressions of the magnetic field $\mathbf{b}^r$ distributions outside a parallelepipedic permanent magnet, which may also be used to estimate the remanent flux inside the magnet. Their analytical expressions are simplified further and presented for completeness in Appendix D. A central assumption in their approach is the *uniformity* of the magnetization in the sample. This assumption

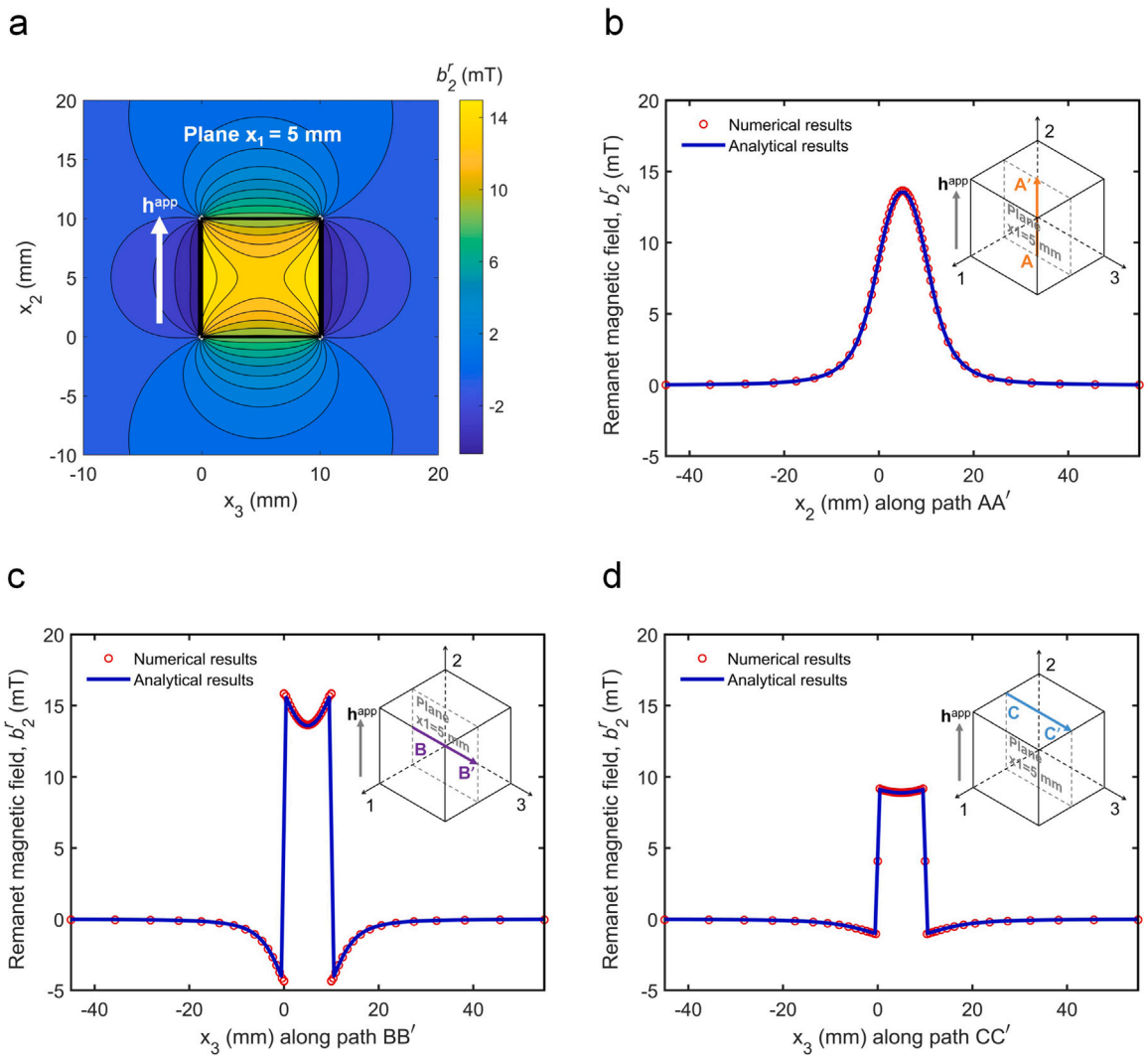

Fig. 12. Comparison between the Gou et al. [64] analytical solutions for a cubic magnet and the present numerical simulations. (a) Contour of the analytical b_2^r component in the central vertical cross-section of the cube and surrounding air. b_2^r profile along the (b) 2-direction and the mid axis, (c) along the 3-direction and the mid axis and (d) along the 3-direction and an axis at the top surface of the cube. The inset sketch shows the direction and position of the plotting directions of b_2^r.

is sufficiently accurate in the present problem as clearly shown in the previous section for cubes and also in Appendix C for different parallelepipeds with various aspect ratios. In that solution, a scalar parameter, denoted as $\widehat{b}^r$, is directly determined by measuring b_2^r at the center of the bottom surface of the sample (measurement presented in Fig. 5d), similarly to the identification of the m_p^s in our full-field model. By comparison with the numerical results, $\widehat{b}^r$ can be directly related to c_p and m_p^s via

$$\widehat{b}^r = \mu_0 \, c_p \, m_p^s. \tag{16}$$

These analytical solutions therefore reproduce readily the numerical results in Fig. 10, whereby they are extremely useful to reconstruct the magnetic flux distributions inside and outside the magnetized domain for a parallelepiped geometry.

Fig. 12 shows a comparison of the Gou et al. [64] analytical solutions and the numerical estimates for the main component b_2^r along different directions. While the solutions of Gou et al. [64] have been obtained to predict $\mathbf{b}^r$ outside a parallelepiped body, by comparison with our numerical simulations, we find that those solutions also hold inside the magnetized body. We find that b_2^r is non-uniform inside the cube, is maximum at its center, vanishes rapidly when moving away from the sample's surface along the 2-direction, and exhibits a strong discontinuity at the cube interface with the surrounding air along the 3-direction, as expected from the Maxwell equations [71,72]. Furthermore, given the fact that the magnetization m_2^r has been shown to be uniform in the present geometry, one can obtain m_2^r according to the continuity of the tangential component of h_2^r at the interface between the air and sample [7].

The agreement between the experimental and analytical estimates is extremely good implying that the *h*-MRE foam behaves indeed as a continuum permanent magnet with "uniform magnetization" (which is one of the principal underlying assumptions of the analytical solution of Gou et al. [64]) allowing to have a quick estimate of the underlying remanent magnetic flux $\mathbf{b}^r$ in the entire sample if the field is known at one location (via measurement). This analytical solution, however, requires re-calibration of the parameter $\widehat{b}^r$ each time the particle content changes and cannot be used for non-parallelepipedic geometries. Yet, one of the potential interests of the *h*-MRE foams and in general of magnetically hard and soft MREs is their potential to be fabricated in various complex shapes [47,73,74].

6. Conclusion

In this study, we fabricate *h*-MRE elastomer foams with different particle contents through an in-situ fabrication process and characterize

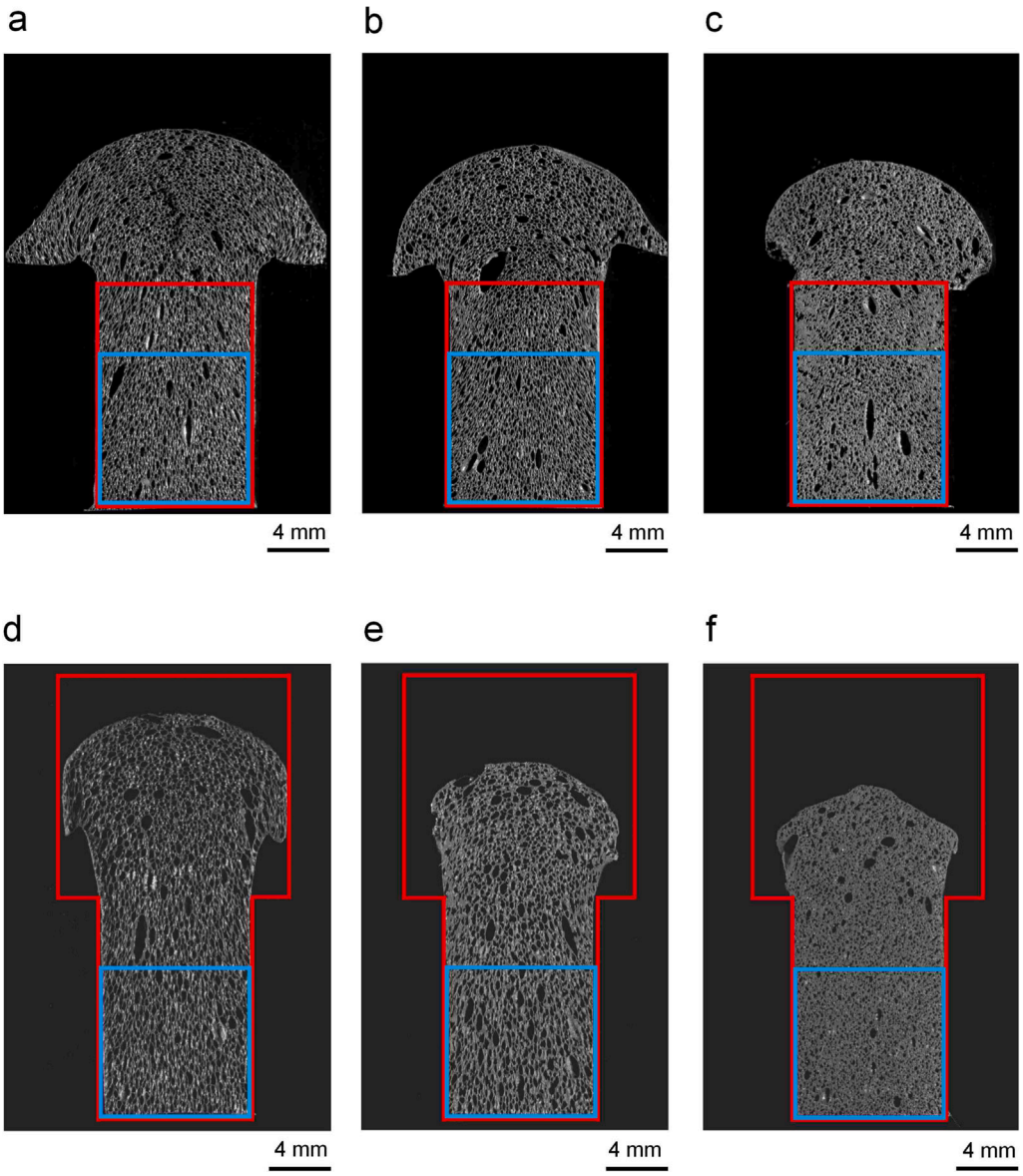

Fig. A.13. Optical micrographs of the vertical cross-sections of *h*-MRE samples of different particle contents fabricated in different molds. Red lines delineate the mold shape and blue lines the considered zone of interest. Mold with a 10 mm × 10 mm cross-section along a 15 mm height for (a) 70 phr, (b) 140 phr, and (c) 210 phr samples. Mold with a 10 mm × 10 mm cross-section along a 15 mm height, followed by a 15 mm × 15 mm cross-section along another 15 mm height for (d) 70 phr, (e) 140 phr, and (f) 210 phr samples.

their pore morphology, size and shape distribution. We observe that the majority of pores exhibits ellipsoidal shapes whereas their size is found to decrease with the increase in particle content. In addition, we find that porosity decreases in general with the increase in particle content.

The analysis of the magnetic properties of the foams shows unambiguously that the void shape (and size) has no effect on the magnetic properties of the foams. In addition, we find that the speed of magnetization does not alter the remanent magnetic flux of the foam. More importantly, we show experimentally that the main parameter controlling the magnetic behavior is the overall particle volume fraction in the *h*-MRE foam, with the remanent magnetic flux being a linear function of the particle volume fraction.

In parallel, we adapt an earlier dissipative homogenization-guided magnetic model proposed for compact incompressible hMREs in the context of hMRE foams taking into account directly the effect of the particle volume fraction and porosity. The explicit model is three-dimensional and is verified via full-field periodic unit-cell simulations of the reconstructed void geometry. In addition, the model has been implemented numerically as a user element in [68]. Note that even though it is employed here on a cube for validation purposes, it can in fact now be used to solve arbitrary BVPs with any complex geometry. The numerical BVP solution combined with the experimental data is used to calibrate a single material constant, the magnetization saturation of the particles. We recover as expected that both the remanent magnetic flux and magnetic field strength are heterogeneous in the cubic specimen, but not the magnetization.

This observation allows to revisit the analytical solution of Gou et al. [64] valid for parallelepiped magnets and show by comparison with the numerical estimates that the solution of the remanent magnetic flux is also valid inside the magnet. This analytical solution allows for a quick estimate of the remanent magnetic flux of parallelepiped *h*-MRE foams only by identifying a single fitting constant. The present study is one of the first in *h*-MRE elastomer foams and focuses on their purely magnetic response, which is a necessary important step towards

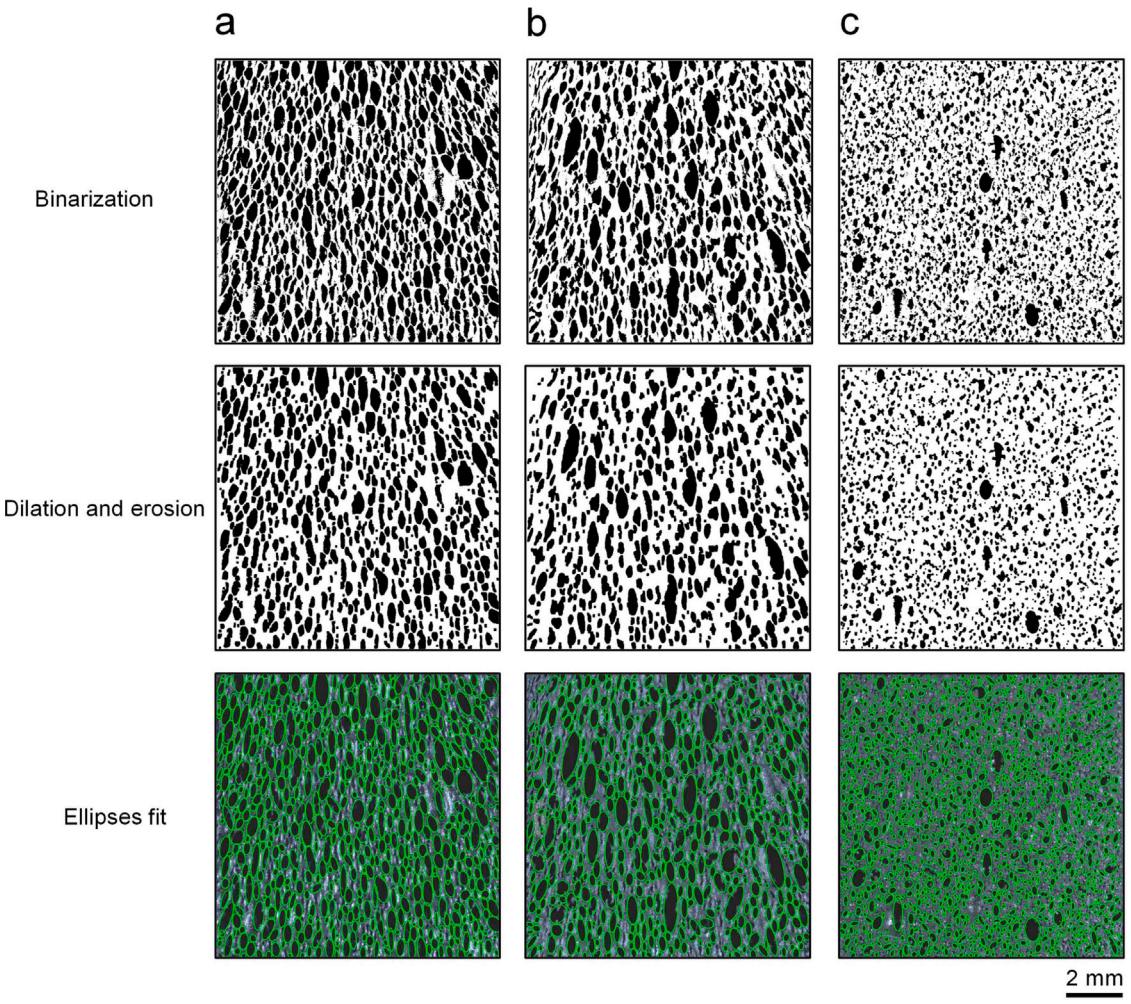

Fig. B.14. Main steps of the image processing of the vertical cross-section micrographs of *h*-MRE foam samples with different particle content: (a) 70 phr (c_v = 0.606, c_p = 0.032), (b) 140 phr (c_v = 0.593, c_p = 0.062), and (c) 210 phr (c_v = 0.413, c_p = 0.124). The vertical axis corresponds to the foaming direction.

understanding their more general magneto-mechanical response. The latter is underway and will be presented elsewhere. The tools developed in the present work may also be extended to study *s*-MRE foams and this again is beyond the scope of the present work.

CRediT authorship contribution statement

Zehui Lin: Writing – review & editing, Writing – original draft, Validation, Methodology, Investigation, Data curation. **Zahra Hooshmand-Ahoor:** Writing – review & editing, Validation, Methodology, Investigation, Data curation. **Kostas Danas:** Writing – review & editing, Supervision, Methodology, Funding acquisition, Conceptualization. **Laurence Bodelot:** Writing – review & editing, Supervision, Methodology, Conceptualization.

Declaration of competing interest

The authors declare that they have no known competing financial interests or personal relationships that could have appeared to influence the work reported in this paper.

Acknowledgments

Zehui Lin acknowledges the China Scholarship Council for his doctoral funding. All authors acknowledge partial support from the European Research Council (ERC) under the European Union's Horizon 2020 research and innovation program (grant agreement No. 101081821). The authors thank Prof. Garcia-Gonzalez and Dr. Lopez-Donaire for useful discussions and for their help in magnetizing some *h*-MRE foam samples with their magnetizer at U. Carlos III, Madrid allowing to complete the data in Fig. 6.

Appendix A. Influence of mold shape on the foam morphology

See Fig. A.13.

Appendix B. Histograms of characteristics of fitted ellipses

We carry out a quantitative image processing of cross-section micrographs using the Python cv2 and scikit-image libraries (Fig. B.14). Lighting is adjusted during imaging so that the voids appear as dark as possible and the *h*-MRE matrix in shades of gray. Using multi-Otsu thresholding, we convert the grayscale image into a binary image in which the voids are intended to appear black and the matrix white. However, the binarized image remains noisy, especially for 70 and 140 phr samples (see Fig. B.14b,c), since isolated black pixels appear in the white matrix phase, thereby reducing the accuracy of pore identification. We improve upon this by applying a dilation operation in the white phase thus filling the isolated black pixels. This step is followed by an erosion operation with the same kernel parameters as for dilation, so that the black voids regain their original size. These two

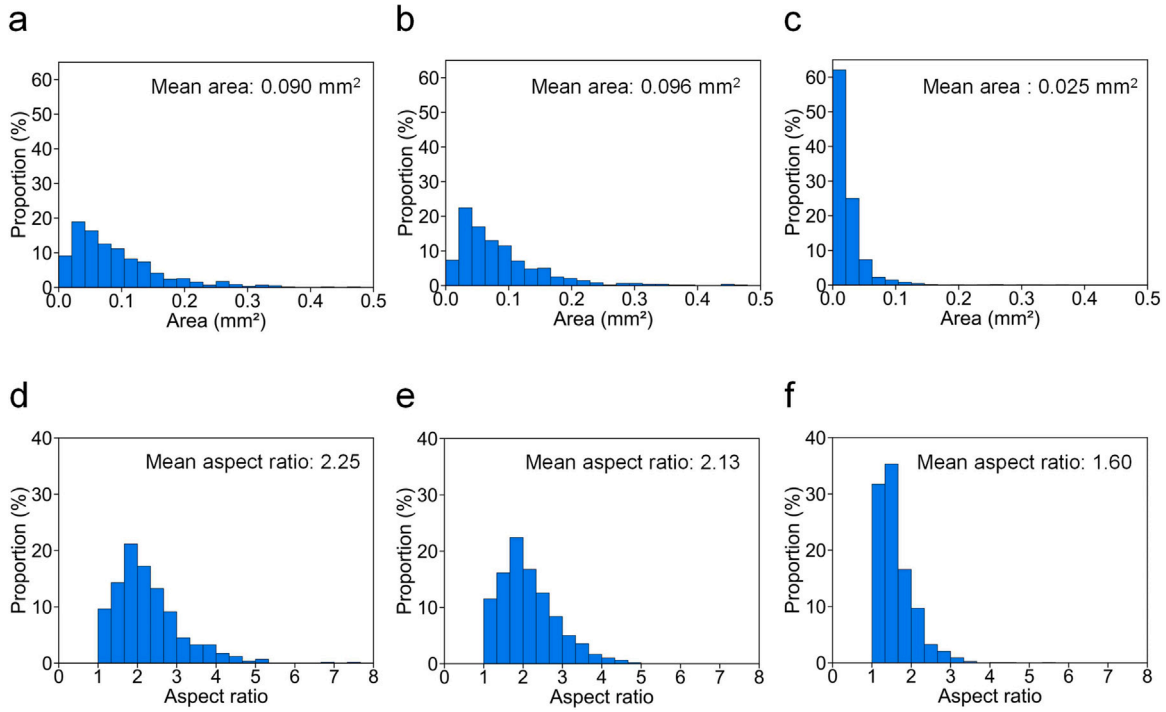

Fig. B.15. Histograms of the void size and shape in the vertical cross-sections shown in Fig. 1. Area of elliptical voids for (a) 70 phr (c_v = 0.606, c_p = 0.032), (b) 140 phr (c_v = 0.593, c_p = 0.062), and (c) 210 phr (c_v = 0.413, c_p = 0.124). Aspect ratios of the elliptical voids for (d) 70 phr, (e) 140 phr, and (f) 210 phr.

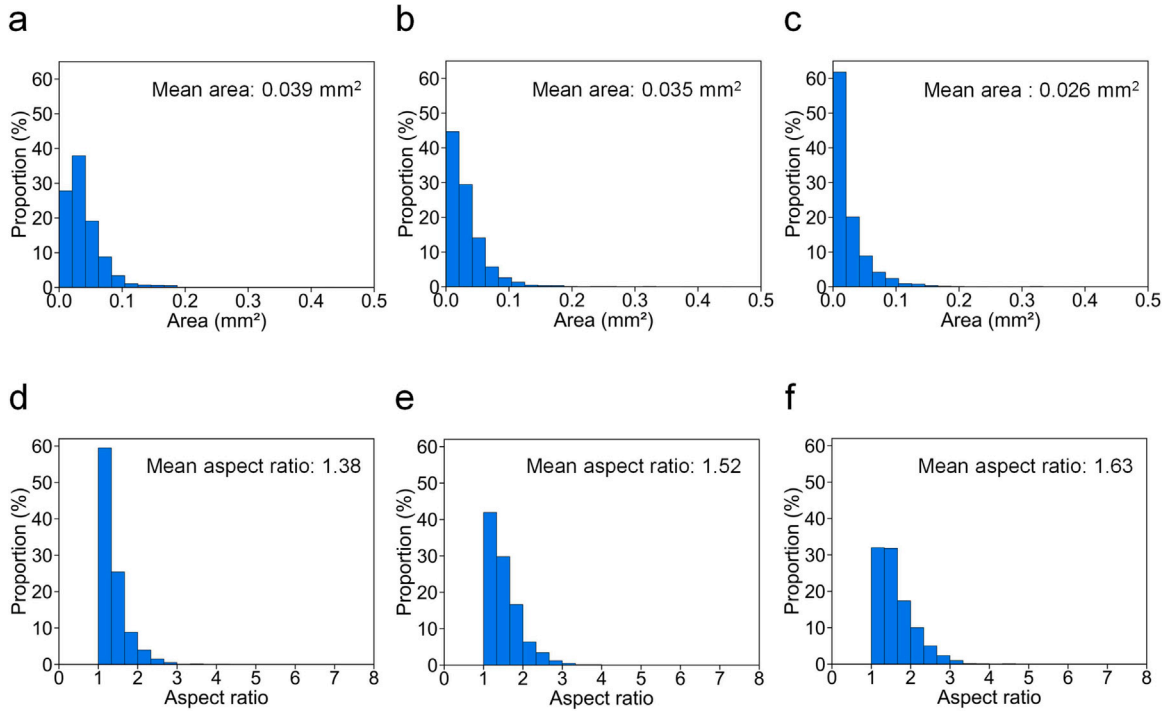

Fig. B.16. Histograms of the void size and shape in the horizontal cross-sections shown in Fig. 1. Area of elliptical voids for (a) 70 phr (c_v = 0.606, c_p = 0.032), (b) 140 phr (c_v = 0.593, c_p = 0.062), and (c) 210 phr (c_v = 0.413, c_p = 0.12). Aspect ratios of the elliptical voids for (d) 70 phr, (e) 140 phr, and (f) 210 phr.

operations allow to eliminate most of the noise in the binary image, as can be seen in Fig. B.14, where the process is illustrated in the case of the vertical cross-sections of Fig. 1. Then, we carry out contour detection to delineate the boundaries between the black phase and the white one, and run ellipse fitting on these boundaries so that the characteristics of the detected ellipses can be analyzed.

Fig. B.15a–c shows the distributions of the measured area of the elliptical voids and Fig. B.15d–f the aspect ratios of the fitted ellipses in the vertical cross-sections. The number of detected voids are 581, 477 and 1229 for samples of 70, 140 and 210 phr, respectively. For the horizontal cross-sections, the distributions of the area of the fitted ellipses is plotted in Fig. B.16a–c, and the aspect ratios in Fig. B.16d–f.

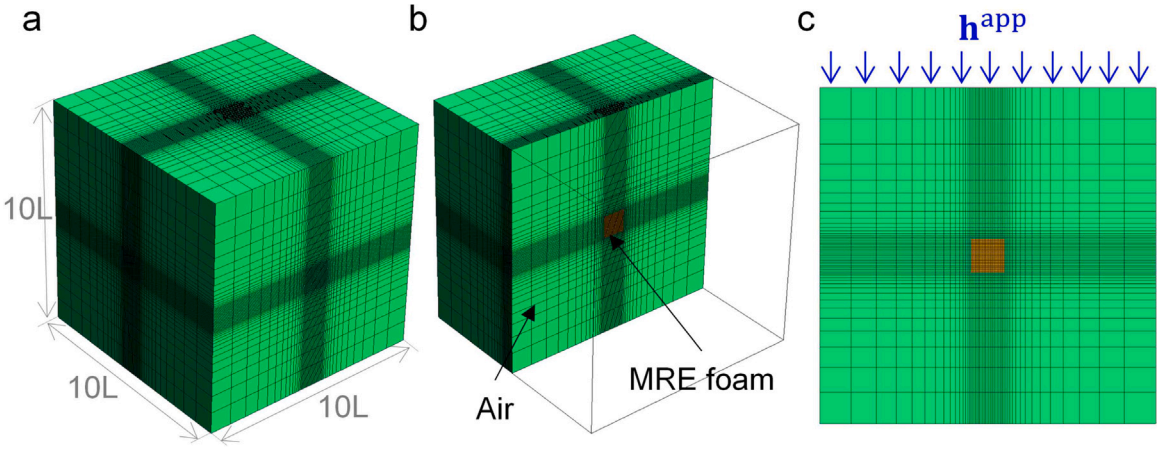

Fig. C.17. (a) The mesh and the computation area for the boundary value problem of *h*-MRE foams. The length of the surrounding air is ten times the length of the *h*-MRE foam sample, (b) a cross-section of the mesh used for the BVP, which includes the *h*-MRE foam cubic sample and the surrounding air, (c) the applied boundary condition of the BVP.

The number of detected voids are in this case 1335, 1498 and 1610 for samples with 70, 140 and 210 phr, respectively. Samples of 70 and 140 phr exhibit very similar characteristics with ellipsoidal voids being elongated in the vertical direction, with average vertical and horizontal aspect ratios of 2.19 and 1.45, respectively. Their size estimated by the area exhibit some polydispersity especially in the vertical cross-section. In contrast, in the case of 210 phr, the void morphology changes significantly with both average vertical and horizontal aspect ratios being close to 1.60, and with void sizes being in general smaller and more monodisperse.

Appendix C. BVP mesh and influence of sample aspect ratio on magnetization uniformity

First, the geometry and mesh of the analyzed boundary value problem (BVP) is reported in Fig. C.17.

Second, to assess whether the shape of the sample affects the uniformity of magnetization, BVPs with identical parameters are run on *h*-MRE uniform foams with varying aspect ratios ranging from 0.1 to 5 (Fig. C.18a). In order to ensure that the results are comparable, the element sizes are kept constant across all aspect ratios. Fig. C.18b shows the remanent fields b_2^r, h_2^r and m_2^r, along with their respective variations throughout the *h*-MRE foam for the different aspect ratios studied. The results demonstrate that increasing the aspect ratio leads to higher b_2^r values, while h_2^r decreases as the sample becomes more elongated. Interestingly, the remanent magnetization, m_2^r, remains constant regardless of the aspect ratio. This indicates that the magnetization behavior is not influenced by changes in the sample's aspect ratio.

For further analysis, the contours of the magnetic fields are examined for samples with the aspect ratios of 0.2 and 5 (Fig. C.18c and d). Even in these highly flattened or elongated configurations, the variations in the magnetic fields are minimal, suggesting that the uniformity of magnetization remains largely unaffected despite substantial changes in aspect ratio.

Appendix D. Analytical solution of Gou et al.

We report the analytical expressions used to evaluate the remanent $\mathbf{b}^r$ field after simplifying slightly the results of Gou et al. [64]. We also note that those expressions are also valid inside the magnet after comparing them with the numerical solutions obtained in this work. Specifically, we consider a magnetized parallelepiped along direction 2 with dimensions $L_1 \times L_2 \times L_3$. Then the remanent magnetic field $\mathbf{b}^r$ in such a magnet may be evaluated up to an unknown constant, denoted here as $\widehat{b}^r$, which may be obtained by measuring any one component of the latter remanent field at one point in space. The remanent field along the magnetized direction 2 reads

$$\begin{aligned} b_2^r(x_1,x_2,x_3) = \frac{\widehat{b}^r}{4\pi}\Big[& F_2(L_1-x_1,L_2-x_2,L_3-x_3)+F_2(L_1-x_1,L_2-x_2,x_3) \\ & +F_2(x_1,L_2-x_2,L_3-x_3)+F_2(x_1,L_2-x_2,x_3) \\ & +F_2(L_1-x_1,x_2,L_3-x_3)+F_2(L_1-x_1,x_2,x_3) \\ & +F_2(x_1,x_2,L_3-x_3)+F_2(x_1,x_2,x_3)\Big] \end{aligned} \tag{D.1}$$

with F_2 being a non-dimensional function of the spatial coordinates given by

$$F_2(f_1,f_2,f_3) = \begin{cases} \arctan\left[\dfrac{f_2\sqrt{f_1^2+f_2^2+f_3^2}}{f_1 f_3}\right], & f_1,f_3 \neq 0 \\ 0, & \text{otherwise.} \end{cases} \tag{D.2}$$

The corresponding components lying at the plane perpendicular to the applied magnetization read

$$\begin{aligned} b_1^r(x_1,x_2,x_3) = \frac{\widehat{b}^r}{8\pi}\Big[& F_{13}(x_1,x_2,L_3-x_3)+F_{13}(x_1,L_2-x_2,x_3) \\ & -F_{13}(x_1,L_2-x_2,L_3-x_3)-F_{13}(L_1-x_1,x_2,x_3) \\ & +F_{13}(L_1-x_1,x_2,L_3-x_3)+F_{13}(L_1-x_1,L_2-x_2,x_3) \\ & -F_{13}(L_1-x_1,L_2-x_2,L_3-x_3)-F_{13}(x_1,x_2,x_3)\Big] \end{aligned} \tag{D.3}$$

$$\begin{aligned} b_3^r(x_1,x_2,x_3) = \frac{\widehat{b}^r}{8\pi}\Big[& F_{13}(x_3,x_2,L_1-x_1)+F_{13}(x_3,L_2-x_2,x_1) \\ & -F_{13}(x_3,L_2-x_2,L_1-x_1)-F_{13}(L_3-x_3,x_2,x_1) \\ & +F_{13}(L_3-x_3,x_2,L_1-x_1)+F_{13}(L_3-x_3,L_2-x_2,x_1) \\ & -F_{13}(L_3-x_3,L_2-x_2,L_1-x_1)-F_{13}(x_3,x_2,x_1)\Big] \end{aligned} \tag{D.4}$$

with F_{13} being a non-dimensional function of the spatial coordinates given by

$$F_{13}(f_1,f_2,f_3) = \begin{cases} \log\left[\dfrac{\sqrt{f_1^2+f_2^2+f_3^2}-f_1}{\sqrt{f_1^2+f_2^2+f_3^2}+f_1}\right], & f_1,f_2,f_3 \neq 0 \\ 0, & \text{otherwise.} \end{cases} \tag{D.5}$$

Data availability

Data will be made available on request.

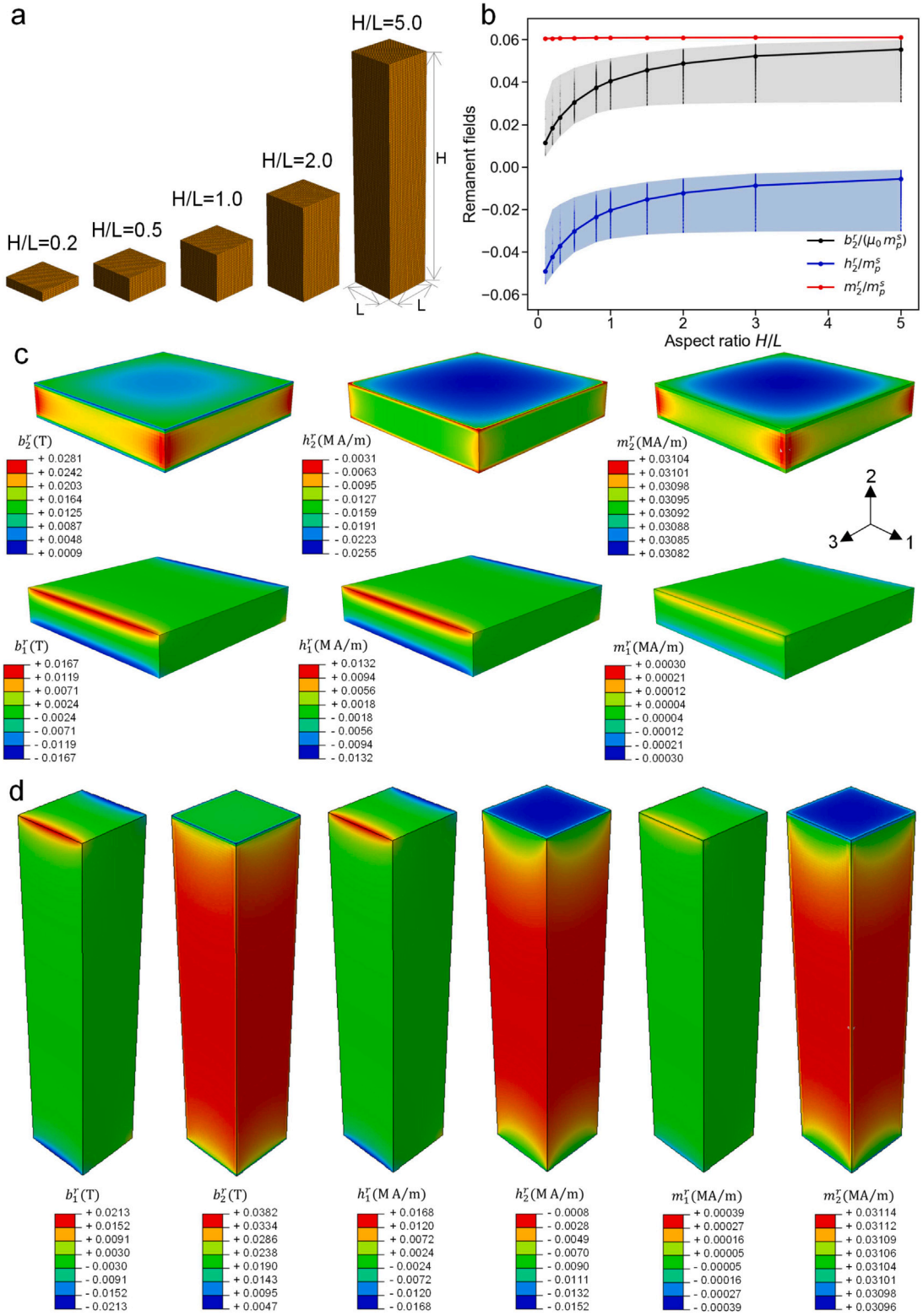

Fig. C.18. The solution of BVP of *h*-MRE foams with different aspect ratios. (a) The *h*-MRE uniform foams with varying aspect ratios H/L, where H is the height of the sample and L is the length. (b) The remanent fields b_2^r, h_2^r and m_2^r and their variation across the *h*-MRE uniform foam at various aspect ratios. The connected dots show the average of the fields. (c) The contours of the local remanent fields b_1^r, b_2^r h_1^r, h_2^r, m_1^r and m_2^r of samples with aspect ratio H/L=0.2 and (d) H/L=5.

References

[1] Z. Rigbi, L. Jilkén, The response of an elastomer filled with soft ferrite to mechanical and magnetic influences, J. Magn. Magn. Mater. 37 (1983) 267–276, http://dx.doi.org/10.1016/0304-8853(83)90055-0.

[2] M.R. Jolly, J.D. Carlson, B.C. Muñoz, T.A. Bullions, The magnetoviscoelastic response of elastomer composites consisting of ferrous particles embedded in a polymer matrix, J. Intell. Mater. Syst. Struct. 7 (1996) 613–622, http://dx.doi.org/10.1177/1045389X9600700601.

[3] J.M. Ginder, S.M. Clark, W.F. Schlotter, M.E. Nichols, Magnetostrictive phenomena in magnetorheological elastomers, I. J. Mod. Phys. B 16 (2002) 2412–2418,

http://dx.doi.org/10.1142/S021797920201244X.
[4] X. Guan, X. Dong, J. Ou, Magnetostrictive effect of magnetorheological elastomer, J. Magn. Magn. Mater. 320 (2008) 158–163, http://dx.doi.org/10.1016/j.jmmm.2007.05.043.
[5] G. Diguet, E. Beaugnon, J. Cavaillé, From dipolar interactions of a random distribution of ferromagnetic particles to magnetostriction, J. Magn. Magn. Mater. 321 (2009) 396–401, http://dx.doi.org/10.1016/j.jmmm.2008.08.112.
[6] K. Danas, S. Kankanala, N. Triantafyllidis, Experiments and modeling of iron-particle-filled magnetorheological elastomers, J. Mech. Phys. Solids 60 (2012) 120–138, http://dx.doi.org/10.1016/j.jmps.2011.09.006.
[7] L. Bodelot, J.-P. Voropaieff, T. Pössinger, Experimental investigation of the coupled magneto-mechanical response in magnetorheological elastomers, Exp. Mech. 58 (2018) 207–221, http://dx.doi.org/10.1007/s11340-017-0334-7.
[8] J. Yao, Y. Sun, Y. Wang, Q. Fu, Z. Xiong, Y. Liu, Magnet-induced aligning magnetorheological elastomer based on ultra-soft matrix, Compos. Sci. Technol. 162 (2018) 170–179, http://dx.doi.org/10.1016/j.compscitech.2018.04.036.
[9] A.K. Bastola, M. Hossain, A review on magneto-mechanical characterizations of magnetorheological elastomers, Compos. Part B Eng. 200 (2020) 108348, http://dx.doi.org/10.1016/j.compositesb.2020.108348.
[10] Y. Qiao, J. Zhang, M. Zhang, L. Liu, P. Zhai, A magnetic field-and frequency-dependent dynamic shear modulus model for isotropic silicone rubber-based magnetorheological elastomers, Compos. Sci. Technol. 204 (2021) 108637, http://dx.doi.org/10.1016/j.compscitech.2020.108637.
[11] L. Ding, S. Zhang, Q. Wang, Y. Wang, S. Xuan, X. Gong, D. Zhang, Self-healing and printable elastomer with excellent shear stiffening and magnetorheological properties, Compos. Sci. Technol. 223 (2022) 109430, http://dx.doi.org/10.1016/j.compscitech.2022.109430.
[12] D. Garcia-Gonzalez, T. Ter-Yesayants, M.A. Mateos, M.L. Lopez-Donaire, Hard-magnetic phenomena enable autonomous self-healing elastomers, Compos. Part B Eng. 248 (2023) 110357, http://dx.doi.org/10.1016/j.compositesb.2022.110357.
[13] S. Leanza, S. Wu, X. Sun, H.J. Qi, R.R. Zhao, Active materials for functional origami, Adv. Mater. 36 (2024) 2302066, http://dx.doi.org/10.1002/adma.202302066.
[14] P. von Lockette, S.E. Lofland, J. Biggs, J. Roche, J. Mineroff, M. Babcock, Investigating new symmetry classes in magnetorheological elastomers: cantilever bending behavior, Smart. Mater. Struct. 20 (2011) 105022, http://dx.doi.org/10.1088/0964-1726/20/10/105022.
[15] G.V. Stepanov, D.Y. Borin, A.V. Bakhtiiarov, P.A. Storozhenko, Magnetic properties of hybrid elastomers with magnetically hard fillers: rotation of particles, Smart. Mater. Struct. 26 (2017) 035060, http://dx.doi.org/10.1088/1361-665X/aa5d3c.
[16] Y. Kim, H. Yuk, R. Zhao, S.A. Chester, X. Zhao, Printing ferromagnetic domains for untethered fast-transforming soft materials, Nature 558 (2018) 274–279, http://dx.doi.org/10.1038/s41586-018-0185-0.
[17] D. Mukherjee, M. Rambausek, K. Danas, An explicit dissipative model for isotropic hard magnetorheological elastomers, J. Mech. Phys. Solids 151 (2021) 104361, http://dx.doi.org/10.1016/j.jmps.2021.104361.
[18] D. Mukherjee, K. Danas, A unified dual modeling framework for soft and hard magnetorheological elastomers, Int. J. Solids St. 257 (2022) 111513, http://dx.doi.org/10.1016/j.ijsolstr.2022.111513.
[19] J.M. Ginder, M.E. Nichols, L.D. Elie, S.M. Clark, Controllable-stiffness components based on magnetorheological elastomers, in: Smart Struct. Mater.: Smart Struct. Integr. Syst, vol. 3985, International Society for Optics and Photonics, SPIE, 2000, pp. 418–425, http://dx.doi.org/10.1117/12.388844.
[20] H.-X. Deng, X.-l. Gong, Application of magnetorheological elastomer to vibration absorber, Commun. Nonlinear Sci. Numer. Simul. 13 (2008) 1938–1947, http://dx.doi.org/10.1016/j.cnsns.2007.03.024.
[21] M. Moreno, J. Gonzalez-Rico, M.L. Lopez-Donaire, A. Arias, D. Garcia-Gonzalez, New experimental insights into magneto-mechanical rate dependences of magnetorheological elastomers, Compos. Part B Eng. 224 (2021) 109148, http://dx.doi.org/10.1016/j.compositesb.2021.109148.
[22] M. Farshad, M. Le Roux, A new active noise abatement barrier system, Polym. Test. 23 (2004) 855–860, http://dx.doi.org/10.1016/j.polymertesting.2004.02.003.
[23] Z. Chen, S. Sun, L. Deng, J. Yang, S. Zhang, H. Du, W. Li, Investigation of a new metamaterial magnetorheological elastomer isolator with tunable vibration bandgaps, Mech. Syst. Signal Pr. 170 (2022) 108806, http://dx.doi.org/10.1016/j.ymssp.2022.108806.
[24] M.A. Moreno-Mateos, J. Gonzalez-Rico, E. Nunez-Sardinha, C. Gomez-Cruz, M.L. Lopez-Donaire, S. Lucarini, A. Arias, A. Muñoz-Barrutia, D. Velasco, D. Garcia-Gonzalez, Magneto-mechanical system to reproduce and quantify complex strain patterns in biological materials, Appl. Mater. Today 27 (2022) 101437, http://dx.doi.org/10.1016/j.apmt.2022.101437.
[25] G.Z. Lum, Z. Ye, X. Dong, H. Marvi, O. Erin, W. Hu, M. Sitti, Shape-programmable magnetic soft matter, P. Natl. Acad. Sci. 113 (2016) E6007–E6015, http://dx.doi.org/10.1073/pnas.1608193113.
[26] M.A. Moreno-Mateos, M. Hossain, P. Steinmann, D. Garcia-Gonzalez, Hybrid magnetorheological elastomers enable versatile soft actuators, Npj Comput. Mater. 8 (2022) http://dx.doi.org/10.1038/s41524-022-00844-1.
[27] S. Lucarini, M. Hossain, D. Garcia-Gonzalez, Recent advances in hard-magnetic soft composites: Synthesis, characterisation, computational modelling, and applications, Compos. Struct. 279 (2022) 114800, http://dx.doi.org/10.1016/j.compstruct.2021.114800.
[28] S. Bednarek, The giant linear magnetostriction in elastic ferromagnetic composites within a porous matrix, J. Magn. Magn. Mater. 301 (2006) 200–207, http://dx.doi.org/10.1016/j.jmmm.2005.05.041.
[29] D. Davino, P. Mei, L. Sorrentino, C. Visone, Polymeric composite foams with properties controlled by the magnetic field, IEEE Trans. Magn. 48 (2012) 3043–3046, http://dx.doi.org/10.1109/TMAG.2012.2198634.
[30] M. D'Auria, D. Davino, R. Pantani, L. Sorrentino, Polymeric foam-ferromagnet composites as smart lightweight materials, Smart. Mater. Struct. 25 (2016) 055014, http://dx.doi.org/10.1088/0964-1726/25/5/055014.
[31] Y. Wang, G. Guo, Y. Zhou, Y. Sun, D. Li, Y. Liu, G. Zhao, Facile synthesis of magnetic rubber foam with cellular structure by one-step solution foam processing for application in giant magnetostriction, Compos. Sci. Technol. 170 (2019) 34–41, http://dx.doi.org/10.1016/j.compscitech.2018.11.023.
[32] B.X. Ju, M. Yu, J. Fu, Q. Yang, X.Q. Liu, X. Zheng, A novel porous magnetorheological elastomer: Preparation and evaluation, Smart. Mater. Struct. 21 (2012) 035001, http://dx.doi.org/10.1088/0964-1726/21/3/035001.
[33] L. Sorrentino, M. Aurilia, G. Forte, S. Iannace, Anisotropic mechanical behavior of magnetically oriented iron particle reinforced foams, J. Appl. Polym. Sci. 119 (2011) 1239–1247, http://dx.doi.org/10.1002/app.32603.
[34] N.S. Muhazeli, N.A. Nordin, S.A. Mazlan, S.A. Abdul Aziz, Ubaidillah, N. Nazmi, Mini review: An insight on the fabrication methods of smart magnetic polymer foam, J. Magn. Magn. Mater. 534 (2021) 168038, http://dx.doi.org/10.1016/j.jmmm.2021.168038.
[35] F. Scarpa, W.A. Bullough, P. Lumley, Trends in acoustic properties of iron particle seeded auxetic polyurethane foam, P. I. Mech. Eng. C- J Mec. 218 (2004) 241–244, http://dx.doi.org/10.1243/095440604322887099.
[36] L. Ge, S. Xuan, G. Liao, T. Yin, X. Gong, Stretchable polyurethane sponge reinforced magnetorheological material with enhanced mechanical properties, Smart. Mater. Struct. 24 (2015) 037001, http://dx.doi.org/10.1088/0964-1726/24/3/037001.
[37] J. Yang, W. Zhang, X. Ge, Preparation and magneto-mechanical properties of 3d microporous magnetorheological foam, J. Intell. Mater. Syst. Struct. 34 (2023) 1305–1313, http://dx.doi.org/10.1177/1045389X221131808.
[38] B.X. Ju, M. Yu, J. Fu, X. Zheng, Q. Yang, Study on the properties of porous magnetorheological elastomers under shock effect, J. Physics: Conf. Ser. 412 (2013) 012039, http://dx.doi.org/10.1088/1742-6596/412/1/012039.
[39] N.S. Muhazeli, N.A. Nordin, U. Ubaidillah, S.A. Mazlan, S.A. Abdul Aziz, N. Nazmi, I. Yahya, Magnetic and tunable sound absorption properties of an in-situ prepared magnetorheological foam, Materials 13 (2020) 5637, http://dx.doi.org/10.3390/ma13245637.
[40] M. Schümann, S. Günther, S. Odenbach, The effect of magnetic particles on pore size distribution in soft polyurethane foams, Smart. Mater. Struct. 23 (2014) 075011, http://dx.doi.org/10.1088/0964-1726/23/7/075011.
[41] M. Schümann, N. Seelig, S. Odenbach, The effect of external magnetic fields on the pore structure of polyurethane foams loaded with magnetic microparticles, Smart. Mater. Struct. 24 (2015) 105028, http://dx.doi.org/10.1088/0964-1726/24/10/105028.
[42] N.S. Muhazeli, N.A. Nordin, S.A. Mazlan, N. Rizuan, S.A. Abdul Aziz, A.Y. Abd Fatah, Z. Ibrahim, U. Ubaidillah, S.-B. Choi, Characterization of morphological and rheological properties of rigid magnetorheological foams via in situ fabrication method, J. Mater. Sci. 54 (2019) 13821–13833, http://dx.doi.org/10.1007/s10853-019-03842-9.
[43] G. Diguet, G. Sebald, M. Nakano, M. Lallart, J.-Y. Cavaillé, Magnetic behavior of magneto-rheological foam under uniaxial compression strain, Smart. Mater. Struct. 31 (2022) 025018, http://dx.doi.org/10.1088/1361-665X/ac3fc8.
[44] Q. Gong, J. Wu, X. Gong, Y. Fan, H. Xia, Smart polyurethane foam with magnetic field controlled modulus and anisotropic compression property, RSC Adv. 3 (2013) 3241, http://dx.doi.org/10.1039/c2ra22824f.
[45] T. Plachy, O. Kratina, M. Sedlacik, Porous magnetic materials based on epdm rubber filled with carbonyl iron particles, Compos. Struct. 192 (2018) 126–130, http://dx.doi.org/10.1016/j.compstruct.2018.02.095.
[46] N.M. Wereley, C. Perez, Y.T. Choi, Strain-dependent dynamic compressive properties of magnetorheological elastomeric foams, Aip Adv. 8 (2018) 056721, http://dx.doi.org/10.1063/1.5007266.
[47] S. Lantean, I. Roppolo, M. Sangermano, M. Hayoun, H. Dammak, G. Barrera, P. Tiberto, C.F. Pirri, L. Bodelot, G. Rizza, Magnetoresponsive devices with programmable behavior using a customized commercial stereolithographic 3d printer, Adv. Mater. Technol. 7 (2022) 2200288, http://dx.doi.org/10.1002/admt.202200288.
[48] D. Mukherjee, K. Danas, An evolving switching surface model for ferromagnetic hysteresis, J. Appl. Phys. 125 (2019) 033902, http://dx.doi.org/10.1063/1.5051483.
[49] A.A. Marzuki, N.A. Nordin, S.A. Mazlan, M.A.F. Johari, R.E. Mohamed Khaidir, M. Sedlacik, Ubaidillah, Enhancement of the rheological properties of magnetorheological foam via different constraint volumes foaming approach, Polym. Test. 128 (2023) 108235, http://dx.doi.org/10.1016/j.polymertesting.2023.108235.

[50] D. Garcia-Gonzalez, M. Moreno, L. Valencia, A. Arias, D. Velasco, Influence of elastomeric matrix and particle volume fraction on the mechanical response of magneto-active polymers, Compos. Part B Eng. 215 (2021) 108796, http://dx.doi.org/10.1016/j.compositesb.2021.108796.

[51] F. Saint-Michel, L. Chazeau, J.-Y. Cavaillé, E. Chabert, Mechanical properties of high density polyurethane foams: I. effect of the density, Compos. Sci. Technol. 66 (2006) 2700–2708, http://dx.doi.org/10.1016/j.compscitech.2006.03.009.

[52] O. Doutres, N. Atalla, K. Dong, Effect of the microstructure closed pore content on the acoustic behavior of polyurethane foams, J. Appl. Phys. 110 (2011) http://dx.doi.org/10.1063/1.3631021.

[53] K. Anoukou, R. Brenner, F. Hong, M. Pellerin, K. Danas, Random distribution of polydisperse ellipsoidal inclusions and homogenization estimates for porous elastic materials, Comput. Struct. 210 (2018) 87–101, http://dx.doi.org/10.1016/j.compstruc.2018.08.006.

[54] O. Zerhouni, M. Tarantino, K. Danas, Numerically-aided 3d printed random isotropic porous materials approaching the hashin-shtrikman bounds, Compos. Part B Eng. 156 (2019) 344–354, http://dx.doi.org/10.1016/j.compositesb.2018.08.032.

[55] J. Segurado, J. Llorca, A numerical approximation to the elastic properties of sphere-reinforced composites, J. Mech. Phys. Solids 50 (2002) 2107–2121, http://dx.doi.org/10.1016/S0022-5096(02)00021-2.

[56] O. Lopez-Pamies, T. Goudarzi, K. Danas, The nonlinear elastic response of suspensions of rigid inclusions in rubber: Ii—a simple explicit approximation for finite-concentration suspensions, J. Mech. Phys. Solids 61 (2013) 19–37, http://dx.doi.org/10.1016/j.jmps.2012.08.013.

[57] O. Zerhouni, S. Brisard, K. Danas, Quantifying the effect of two-point correlations on the effective elasticity of specific classes of random porous materials with and without connectivity, Internat. J. Engrg. Sci. 166 (2021) 103520, http://dx.doi.org/10.1016/j.ijengsci.2021.103520.

[58] K. Danas, Effective response of classical, auxetic chiral magnetoelastic materials by use of a new variational principle, J. Mech. Phys. Solids 105 (2017) 25–53, http://dx.doi.org/10.1016/j.jmps.2017.04.016.

[59] M. Tarantino, O. Zerhouni, K. Danas, Random 3d-printed isotropic composites with high volume fraction of pore-like polydisperse inclusions and near-optimal elastic stiffness, Acta Mater. 175 (2019) 331–340, http://dx.doi.org/10.1016/j.actamat.2019.06.020.

[60] Z. Hooshmand-Ahoor, M. Tarantino, K. Danas, Mechanically-grown morphogenesis of voronoi-type materials: Computer design, 3d-printing and experiments, Mech. Mater. 173 (2022) 104432, http://dx.doi.org/10.1016/j.mechmat.2022.104432.

[61] Z. Hooshmand-Ahoor, H. Luo, K. Danas, M-voronoi and other random open and closed-cell elasto-plastic cellular materials: Geometry generation and numerical study at small and large strains, Int. J. Solids St. 290 (2024) 112680, http://dx.doi.org/10.1016/j.ijsolstr.2024.112680.

[62] C. Perez-Garcia, J. Aranda-Ruiz, M.L. Lopez-Donaire, R. Zaera, D. Garcia-Gonzalez, Magneto-responsive bistable structures with rate-dependent actuation modes, Adv. Funct. Mater. 34 (2024) 2313865, http://dx.doi.org/10.1002/adfm.202313865, URL: https://advanced.onlinelibrary.wiley.com/doi/abs/10.1002/adfm.202313865, arXiv:https://advanced.onlinelibrary.wiley.com/doi/pdf/10.1002/adfm.202313865.

[63] M.I. Idiart, K. Danas, P. Ponte Castañeda, Second-order theory for nonlinear composites and application to isotropic constituents, C. R. Méc. 334 (2006) 575–581, http://dx.doi.org/10.1016/j.crme.2006.06.006.

[64] X.-F. Gou, Y. Yang, X.-J. Zhen, Analytic expression of magnetic field distribution of rectangular permanent magnets, Appl. Math. Mech. 25 (2004) 297–306, http://dx.doi.org/10.1007/BF02437333.

[65] C.M. Landis, Fully coupled, multi-axial, symmetric constitutive laws for polycrystalline ferroelectric ceramics, J. Mech. Phys. Solids 50 (2002) 127–152, http://dx.doi.org/10.1016/s0022-5096(01)00021-7.

[66] W. Karush, Minima of functions of several variables with inequalities as side constraints, 1939, URL: http://pi.lib.uchicago.edu/1001/cat/bib/4111654.

[67] H.W. Kuhn, A.W. Tucker, Nonlinear programming, Berkeley Symp. Math. Stat. Prob. (1951) 481–492.

[68] ABAQUS, CAE/2017, Simulia, RI, USA, 2023.

[69] D. Mukherjee, M. Rambausek, K. Danas, Abaqus UEL subroutine for hard and soft magnetorheological elastomers, 2021, http://dx.doi.org/10.5281/zenodo.4588578.

[70] M. Rambausek, D. Mukherjee, K. Danas, Supplementary material to a computational framework for magnetically hard and soft viscoelastic magnetorheological elastomers, 2021, http://dx.doi.org/10.5281/zenodo.5543516.

[71] A. Dorfmann, R. Ogden, Magnetoelastic modelling of elastomers, Eur. J. Mecha-A- Solid 22 (2003) 497–507, http://dx.doi.org/10.1016/s0997-7538(03)00067-6.

[72] S. Kankanala, N. Triantafyllidis, On finitely strained magnetorheological elastomers, J. Mech. Phys. Solids 52 (2004) 2869–2908, http://dx.doi.org/10.1016/j.jmps.2004.04.007.

[73] L. Brusa da Costa Linn, K. Danas, L. Bodelot, Towards 4d printing of very soft heterogeneous magnetoactive layers for morphing surface applications via liquid additive manufacturing, Polymers 14 (2022) http://dx.doi.org/10.3390/polym14091684.

[74] M.L. Lopez-Donaire, G. de Aranda-Izuzquiza, S. Garzon-Hernandez, J. Crespo-Miguel, M. Fernandez-de la Torre, D. Velasco, D. Garcia-Gonzalez, Computationally guided diw technology to enable robust printing of inks with evolving rheological properties, Adv. Mater. Technol. 8 (2023) 2201707, http://dx.doi.org/10.1002/admt.202201707.